Beam physics design of a superconducting linac

Zhi-Jun Wang,[1,2,3] Shu-Hui Liu,[1,2,3,†] Wei-Long Chen,[1,2,3] Wei-Ping Dou,[1,2,3] Yuan-Shuai Qin,[1,3] Yuan He,[1,2,3,*] Yong-zhi Jia,[1,3] Chi Feng,[1,2,3] Man Yi,[1,3] Yi-Meng Chu,[1,2,3] Duan-Yang Jia,[1,2,3] Jun-Ren Huang,[1,3] and Hong-Wei Zhao[1,3]

[1]*Institute of Modern Physics, Chinese Academy of Sciences, Lanzhou 73000, China*
[2]*Advanced Energy Science and Technology Guangdong Laboratory, Huizhou 516001, China*
[3]*University of Chinese Academy of Sciences, Beijing 100049, People's Republic of China*

(Received 2 February 2023; accepted 31 October 2023; published 18 January 2024)

The China initiative Accelerator-Driven subcritical System (CiADS) project aims to design and build the world's first accelerator-driven subcritical system demonstration facility. The facility will attain 2.5 MW thermal power in 2026 to realize accelerator-target-reactor coupling experiments. As the first approved accelerator-driven subcritical system facility, the CiADS driver linac will adopt cutting-edge accelerator technologies to achieve the challenging goals of high beam power and high reliability. The accelerator will operate in cw mode to produce a 500 MeV, 5 mA proton beam. To meet the extremely high demands on beam availability, the linac design lays strong emphasis on beam loss control and increased fault tolerance via a novel fault-compensation method. The accelerator complex consists of a room temperature front-end section, a main linac that employs superconducting accelerator technologies, and a high-energy beam transport line. The beam-loss-oriented beam dynamics design of the driver linac complex is presented in the paper.

DOI: 10.1103/PhysRevAccelBeams.27.010101

I. INTRODUCTION

Driven by national demands for the safe disposal of nuclear waste and its potential to breed high-performance nuclear fuel, accelerator-driven subcritical system (ADS) was proposed years ago as one of the technological paths toward a cleaner nuclear power source [1–3]. The China ADS (C-ADS) program, which is planned in four stages, aims to design and build an ADS demonstration facility whose thermal power capacity exceeds 1000 MW in multiple phases lasting about 20 years. The stage by stage development roadmap in Fig. 1 shows how the C-ADS will be implemented in four major phases: Research and development (R&D) phase by 2018, experimental phase by 2026, demo transmutation facility by 2030, and industrial facility by the late 2030s.

The Chinese Academy of Sciences (CAS) initiated the first phase of the C-ADS program in 2011 under the framework of the "Strategic Technology Pilot Project." The program, named "Future Advanced Nuclear Fission Energy," aimed to acquire three key technologies including high power superconducting proton linac, heavy metal spallation target, and subcritical nuclear reactor [4,5]. The program was completed and accepted with a pulsed beam of 25 MeV in energy, 10 mA in current, and cw (continuous wave) beam of 18 MeV in energy, 2.2 mA in current. In this initial stage, critical accelerator technologies, including cw operational radio-frequency quadrupole (RFQ) cavity, low β superconducting cavity, and cryostat, were demonstrated.

As the second stage of the C-ADS program, CiADS plans to realize the accelerator-target-reactor coupling experiments and nuclear waste transmutation study. The CiADS driver linac is designed to accelerate 5 mA proton beam to 500 MeV in cw mode. As shown in Fig. 2, the linac mainly consists of a normal conducting front-end section, a superconducting (SC) acceleration section, and a high-energy beam transport (HEBT). The front end is composed of an electron cyclotron resonance (ECR) ion source, a low energy beam transport (LEBT) containing a fast chopper for beam pulse structuring and machine protection, a radio-frequency quadrupole (RFQ) linac, and a medium energy beam transport (MEBT). The SC section accelerates protons from 2.1 to 500 MeV. The previous design version in 2019 [6] utilized half wave resonators (HWRs), spoke resonators, and elliptical structures. Further considerations on the technological feasibility led to a new scheme in 2022 where only HWR structures and elliptical structures were employed. The HEBT is designed to deliver either a 2.5 MW proton beam to a bending beam line to reactor

*hey@impcas.ac.cn
†liush@impcas.ac.cn

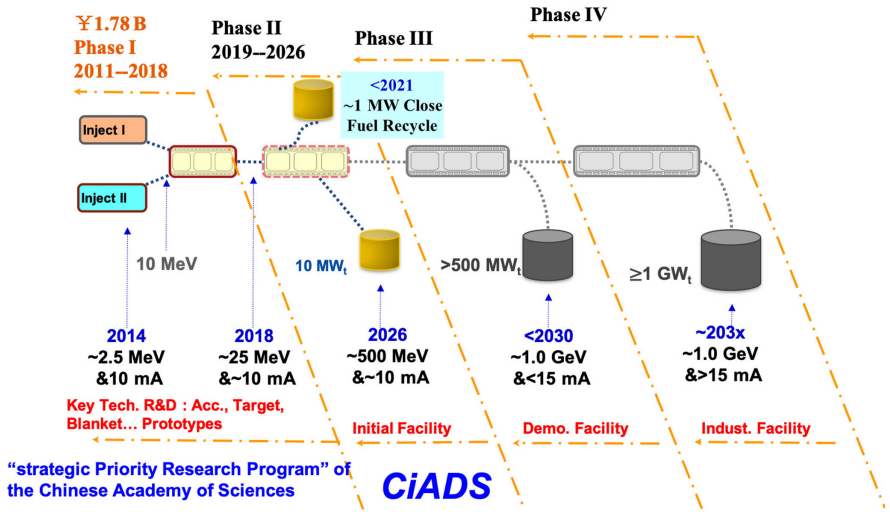

FIG. 1. A roadmap for developing ADS facilities in China.

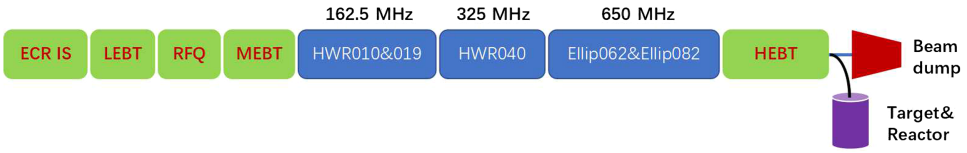

FIG. 2. A layout of the CiADS driver linac.

(BLR) section, or a low power beam, during commissioning, to a straight beam dump that can sustain one-tenth of the maximum beam power. The space to house another ten cryomodules is reserved in the HEBT to readily increase the energy to 1 GeV. Preliminary top-level parameters of the CiADS linac are specified in Table I.

In this paper, general design considerations and main parameter choices of the superconducting cw proton linac are briefly introduced in Sec. II. The beam dynamics design of each section is described in detail in Sec. III. Beam loss in the whole linac is analyzed systematically in Sec. IV. The novel fault compensation method and its application on CiADS linac are presented in Sec. V. The paper concludes with a summary of the beam physics design in Sec. VI.

TABLE I. The top level requirements and parameters of CiADS linac [1].

Parameters	Description
Beam energy	500 MeV (upgrade to 1 GeV)
Beam current	5 mA (upgrade to 10 mA)
Operation mode	cw and pulse
Beam stability	±1% @100 ms for energy ±2% @100 ms for intensity 1 mm @100 ms for centroid
Beam loss	≤ 1 w/m
Beam availability	>80% @3 months
Beam operation cycle	3–9 months per year
Beam trips @time ≤ 10 s	Unlimited
Beam trips @time 10 s–5 min	2500
Beam trips @time ≥ 5 min	300

II. GENERAL CONSIDERATIONS AND MAIN PARAMETER CHOICES

Unlike the traditional accelerator based experimental facility, the CiADS driver linac has very strict requirements on operation availability imposed by the downstream target and reactor system. The reactor demands beam trips to be resolved on a timescale of seconds, which is the most challenging issue for the linac. There are no existing cw proton linacs with similar beam power levels for reference. Meanwhile, several proposed cw proton or deuteron linac projects, such as PIP II [7,8], MYRRHA [9] and IFMIF [10], etc., are good models for the physics design and technical design of the accelerator. What is more, some operating or underconstruction accelerator facilities that use superconducting cavities, such as SNS [11], Facility for Rare Isotope Beams (FRIB) [12], and ESS [13], etc., also serve as a valuable reference for the choice of some critical parameters of hardware systems. This section describes general considerations on the whole driver linac, the beam physics design philosophy, and the choice of key parameters of main hardwares.

A. General design considerations

As an essential performance goal for CiADS, reliability assumes central importance in the design of the SC linac. To meet the stringent requirements, the overall design follows the RAMI (reliability, availability, maintainability, inspectability) principle [14], which is widely used in the field of nuclear energy and aviation, to improve the systematic reliability of the accelerator complex.

1. Reliability

The reliability of hardwares is the foundation of the whole accelerator system. Redundancy and standardized design are basic strategies to increase the said reliability. Key elements such as superconducting cavities and magnets were designed to operate at 80% of their full capacities. Such an arrangement will reduce the probabilities of faults and reserve large parameters for the implementation of fault-compensation schemes. In particular, for the SC cavities in cw mode, the operation voltages were optimized according to the experience of existing SC accelerators. Standardized design was adopted by systems of rf amplifiers and magnet power supplies, which are the main source of machine failure [15–17]. The CiADS linac will use solid-state amplifiers and modular power supplies integrated with standard units.

2. Availability

The design treated the availability of the driver linac as a high-level systematic problem. In addition to the spare hardwares and redundancies by design, fast beam recovery in one second with a compensation scheme is an effective way to improve the beam availability [18]. In this scheme, the artificial intelligence technology under development has the potential to realize the beam recovery. Also, the machine protection system (MPS) should strike a balance between beam availability and machine safety.

3. Maintainability

The maintainability is quite critical for the high-availability superconducting proton linac. First, the average uncontrolled beam loss must be limited to below 1 W/m level to facilitate hands-on maintenance [19]. In the beam dynamics design, the aperture radius in the room temperature section is smaller than that in the superconducting section—this helps eliminate beam loss in the cold section to keep the low temperature elements clean. Second, the hardware should be placed in the warm section and low radiation area to increase the maintenance possibility. Mechanical designs should also be easy to dismount and assemble. Third, online performance recovery technologies of superconducting cavities were developed to shorten the maintenance intervals.

4. Inspectability

Inspectability involves both beam diagnostics and monitoring of the hardware system. Sufficient online beam diagnostics devices must be installed to enable beam tuning up to target beam power. What is more, such devices will be used to offer the key signals to realize fast beam recovery. Hardware systems, e.g., high-voltage rf systems, must be inspectable at some critical locations to help detect potential problems. Timely resolution of such problems will avoid accidents that can cause long-term shutdown of the linac.

B. Beam physics design philosophy

Most of the design philosophy for high-intensity linacs has been addressed by previous literature which includes contributions from SNS [20], ESS [21], IFMIF [22], and so on. Being a 5 mA, 500 MeV cw proton machine, the CiADS linac can be characterized as an emittance dominated high-power superconducting accelerator complex.

III. BEAM PHYSICS DESIGN OF DIFFERENT SECTIONS

Beam loss control is the most challenging issue and the ultimate optimization goal. Beam halo, caused by nonlinear effects such as space-charge effects and nonlinear rf fields, is the main source of beam loss.

A. Room temperature front-end section

The room temperature front end consists of an LEBT, an RFQ, and an MEBT. Its main function is to deliver a high-quality beam by minimizing beam halo in both the transverse and longitudinal phase spaces.

A bending LEBT was designed to improve the transverse beam quality by scraping the outer particles and impure ions H^{2+} and H^{3+}. A chopper was available to generate temporal structure and diagnostics were included to characterize the beam distribution. A collimation scheme was proposed to scrape the outside particles just at the end of the ion source to achieve a good transverse beam distribution.

The four-vane type radio-frequency quadrupole (RFQ) accelerator was designed to accelerate the proton beam from 20 keV to 2.1 MeV within 5 m. High transmission ratio and low longitudinal emittance were critical optimization objectives that facilitated reliable operation and beam loss control in the downstream superconducting section. The input energy and general bunch section were carefully optimized to achieve favorable results. The 99.99% longitudinal emittance was 3.5π mm mrad at an acceleration efficiency of up to 99.3%.

The MEBT serves the following functions: beam reconstruction, halo scraping, and beam matching. The MEBT was designed to achieve smooth matching between the two adjacent accelerating sections. Beam instrumentation in the MEBT will enable phase space reconstruction

TABLE II. Main rf parameters of the CiADS SC linac [24].

	HWR010 [25]	HWR019	HWR040	Ellip062 [26]	Ellip082 [26]
Freq (MHz)	162.5	162.5	325	650	650
β_{opt}	0.10	0.19	0.40	0.62	0.82
Number of cell	2	2	2	6	5
Aperture diameter (mm)	40	40	50	100	100
Epeak (MV/m)	26	28	28	29	29

experiments. Halo elimination was implemented with scrapers separated by certain phase advances.

B. Superconducting acceleration section

An SC acceleration section including three families of SC cavities was designed to accelerate a 10-mA proton beam to 500 MeV. The beam loss was controlled to be lower than 1 W/m strictly. The 90 deg. phase advance limit at zero current and beam matching among different sections were observed to suppress the formation of beam halo [23]. The phase advance was kept smooth while maintaining acceleration efficiency. In view of the uniformity and feasibility in the engineering implementation, the lengths of cryostats in all five sections were determined to be less than 6 m. The main rf characteristics of the SC linac accelerating cavities are summarized in Table II.

C. Accelerator to beam dump

The HEBT was designed as a doublet lattice to deliver the proton beam to a 300 kW test beam dump. A space beyond 100 m in length was reserved for the upgrade plan in the next stage. Beam transportation in the HEBT was demonstrated with beam dynamics simulations.

1. LEBT

Designed to match the 20 keV proton beam of the electron cyclotron resonance (ECR) ion source with the downstream radio-frequency quadrupole (RFQ) accelerator, the low energy beam transport (LEBT) also plays a key role in beam quality control and machine protection. The proton beam produced by the electron cyclotron resonance ion source carries unwanted H_2^+ and H_3^+ ions, which may transport to the RFQ accelerator [27] and lead to cavity arc or radio trip, or even induce instabilities in cavity operation. Therefore, instead of a straight line, the LEBT design of CiADS adopted a bending structure to remove unwanted ion species, thereby purifying the proton beam. In order to improve the matching ability of the LEBT, three solenoids, and one bending magnet were selected for the RFQ matching. The bend angle in the rotation plane will be 20° and the pole face rotation angle will be 6.4°. to separate unwanted ion species and to ensure that the beam would enter the RFQ accelerator symmetrically. Meanwhile, complete beam diagnostic instruments will be installed in the LEBT segment to measure beam parameters accurately and to reduce the mismatch between the LEBT and the RFQ. Two sets of Faraday cups (FC), installed before and after the bending magnetic, respectively, will measure the beam current and act as a beam stop during beam commissioning. A fluoresce view screen (FVS) will be set to calibrate the beam profile and centroid. An Allison scanner will be available downstream of the second solenoid to measure the emittance of the purified proton beam. The dc current transformers (DCCT) and the ac current transformers (ACCT) will be used to monitor the beam intensity in continuous wave or pulse mode, respectively. The LEBT will also equipped with a fast chopper to control the duty factor during beam commissioning and to implement machine protection. To improve high-intensity beam transport, the chopper will be placed at the RFQ entrance to shorten the length where space-charge compensation is absent. The layout of LEBT is shown in Fig. 3.

As the beam focusing is far weaker in the LEBT than in the RFQ accelerator, i.e., the RFQ has a higher phase advance, a relatively compact focusing lattice near the interface can facilitate beam matching. The compact space in front of the RFQ entrance is also conducive to beam envelope compression which helps avoid nonlinear effects from the solenoid. Despite the above considerations, strong space-charge effects of the high-intensity beam can still cause phase space filamentization by the end of the LEBT. The beam extracted from the ECR ion source is assumed without coupling for the 2.45 GHz resonator before the solenoid magnet filed. So one adjusting iris is used to scrape the unwanted particles situated at large beam envelop with large beam divergence. This method named

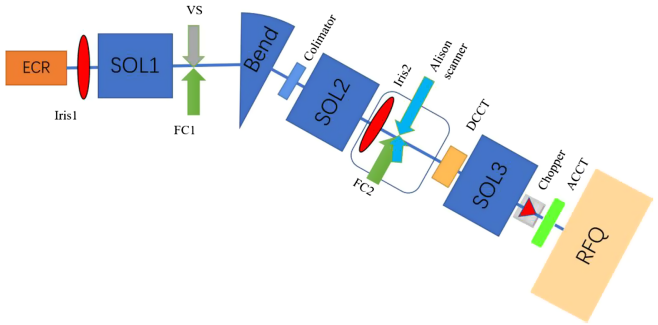

FIG. 3. Layout of CiADS LEBT.

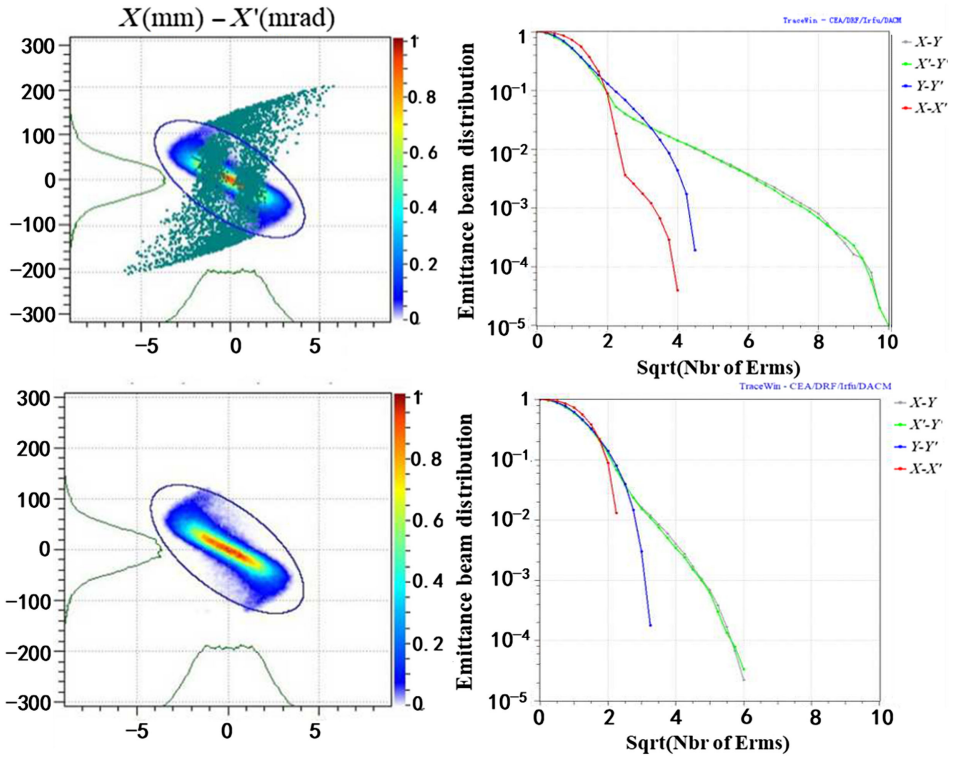

FIG. 4. Beam phase space and beam distribution.

"point light source beam scraping" was applied to optimize beam emittance in the LEBT design of CiADS.

TraceWin [28] code was used for particle tracking. The initial particle distribution out of the ion source was assumed to be a 4D Gaussian distribution with transverse rms emittance of 0.18 mm mrad, and the total particle number was 100 000, and the space-charge compensating factor was set at 0.87 along the LEBT except that of 0 in the banding magnet based on the study results of other accelerator in the world. Tracking results showed that Iris1 can effectively scrape out the filamentation particles in phase space without affecting the beam core. Figure 4 presents the beam phase space and emittance distribution with (top) and without (below) scraper at the exit of LEBT. After the beam scraping, the beam size is decreased from 10 to 6 rms and the distortion of phase space is reduced obviously.

Simulation results led to the following plan for LEBT beam commissioning, which will be revised based on beam measurements. Iris1 will be expected to scrape out about 30% of beam particles from the ion source to improve the beam quality. The collimator will be used to eliminate H_2^+ and H_3^+ particles after the bending magnet. Iris2 will adjust the beam intensity smoothly for beam power ramping in cw mode. Figure 5 presents the beam envelope evolution. The chopper with a 20-ns rise time will be used to generate a pulsed beam with the designated duty cycle. These planned procedures were adopted to ensure the matching of a high-quality beam into the RFQ accelerator.

2. RFQ

The four-vane type radio-frequency quadrupole (RFQ) accelerator was designed to accelerate the proton beam from 20 keV to 2.1 MeV within 4.9 m. As the first longitudinal component, RFQ converts the continuous beam into bunches and determines the longitudinal emittance. The output beam quality of the RFQ, especially the longitudinal emittance, has a significant impact on beam transmission in the superconducting linac.

The critical optimization objectives were reliable operation and beam loss control in the downstream superconducting section. New requirements were raised regarding the CiADS RFQ design after the end-to-end simulation study of the RFQ and the superconducting linac

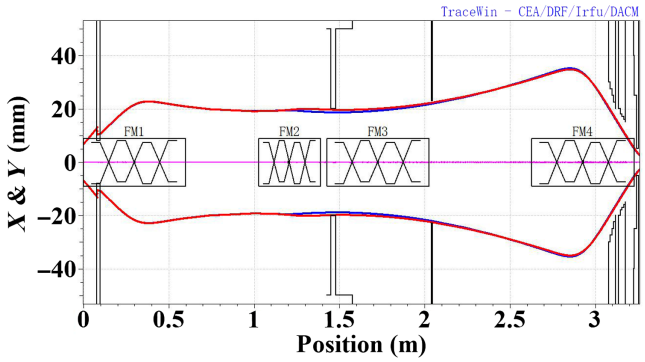

FIG. 5. The beam envelope of LEBT (3 rms).

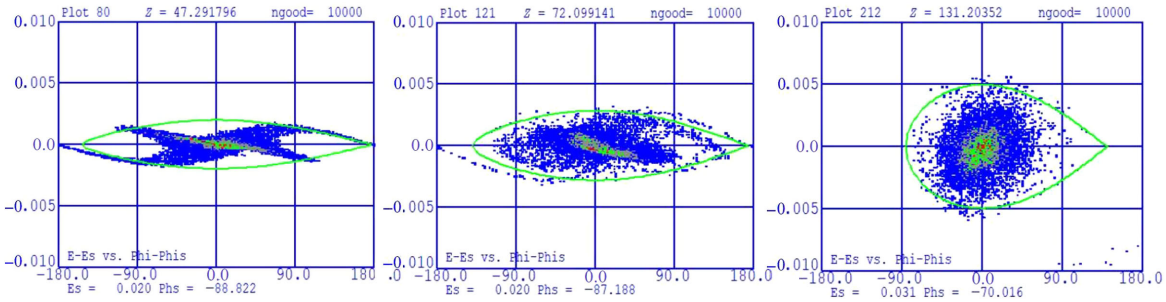

FIG. 6. Beam phase spaces and longitudinal acceptances at cell 80, 121, and 212.

[29]: (i) To maintain long-term steady operation, the maximum surface electric field of the 162.5 MHz RFQ should be less than 17.66 MV/m in cw mode, namely $kp = 1.3$. (ii) To achieve high acceleration efficiency in the superconducting section, the rms longitudinal emittance of the RFQ output beam should be less than 0.22π mm mrad when the beam current is below 5 mA. (iii) To decrease beam loss probabilities in the superconducting section, the 99.99% longitudinal emittance of the output beam should not surpass 0.2 times the acceptance of the superconducting section which was equal to 5.4 mm mrad. Also, the low energy particles should be separated from the main bunch and the proportion of the medium energy particles should be lower.

There were two crucial processes in the full particle optimization design. One was fine optimization of shaper section (SH). Another was to optimize the longitudinal acceptance of all particles in Genter buncher section (GB) in which the 99.99% longitudinal emittance was the main optimization goal.The PARMTEQM code was used for the beam dynamics design of the RFQ [30].

SH is the most crucial section that determines the beam emittance and quality [31]. A better control of the beam emittance and quality, when the beam is shaped, can be achieved through fine optimization of SH. The beam phase space distributions at cell 80, 121, and 212 are shown in Fig. 6. Fine control of SH can be seen from the relationship between phase space and acceptance. At the beginning of SH, there were 24 cells whose $m = 1$ and $\varphi = -90°$ to achieve stable acceptance of the beam. Then, the modulation m and the synchronous phase φ were finely adjusted till the four horns of the beam were gradually dispersed. At cell 121, $m = 1.087$, $\varphi = -87.2°$ and at cell 212, m slowly changed to 1.17, while φ shrank to $-70°$, so that the longitudinal acceptance was optimized to achieve a phase space without obvious distortion.

GB is another crucial part that affects the beam quality. It optimizes the longitudinal acceptance of all particles with the aim of minimizing the 99.99% longitudinal emittance. The beam phase space distributions at cell 241, 276, and 323 are shown in Fig. 7. The synchronous phase and modulation were alternately optimized after SH was finely controlled. The synchronous phase was optimized first till cell 241, the modulation gradually changed to 1.21, and the synchronous phase shrank quickly to $-54°$. Then the modulation was optimized till cell 276, modulation ramped up to 1.95, and the synchronous phase slowly shrank to $-24°$. After the longitudinal acceptance optimization of GB, the beam with small rms and 99.99% longitudinal emittance was obtained at cell 323.

Through the full particle optimization design, the rms longitudinal emittance was 0.209π mm mrad. The 99.99% longitudinal emittance was 4.45π mm mrad at an acceleration efficiency of up to 99.5%. The separation of low energy particles and the main bunch was achieved. The number of simulated particles was 1×10^6. The longitudinal phase space of the output beam with low energy particles is shown in Fig. 8. We can see that the output beam consists of a main bunch and some low-energy dispersed particles. No medium energy particle was found when we analyzed the energy spectrum.

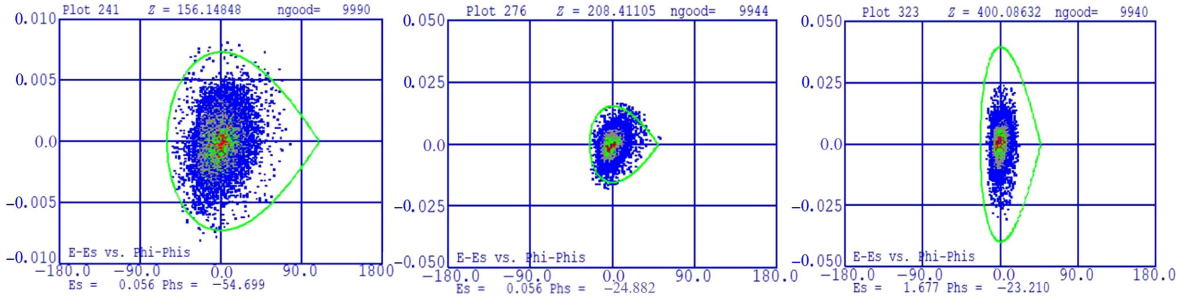

FIG. 7. Beam phase spaces and longitudinal acceptances at cell 241, 276, and 323.

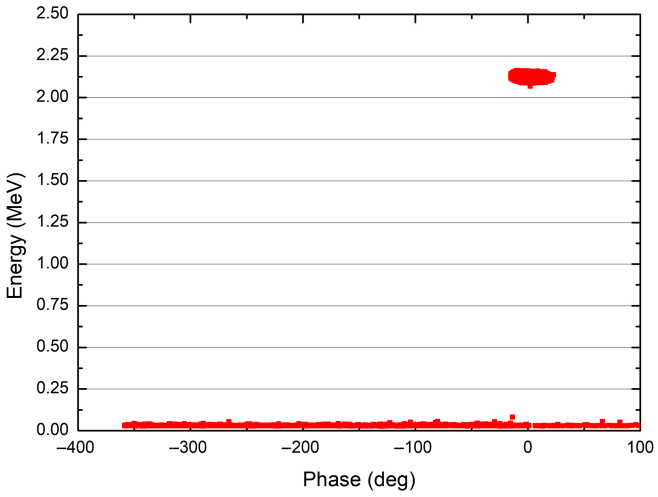

FIG. 8. Longitudinal beam phase space out of RFQ after full particle optimization.

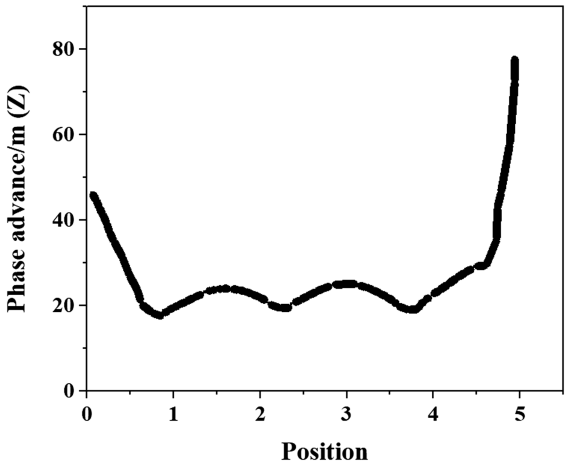

FIG. 10. Longitudinal phase advance curve of MEBT.

3. MEBT

The medium energy beam transport (MEBT) downstream of the RFQ houses focusing elements that match the 2.1 MeV beam into the subsequent superconducting section. The MEBT was designed with great emphasis on smooth matching between the upstream and downstream acceleration sections, beam diagnostics layout, and beam quality control. The design proposed and successfully implemented ways to minimize the phase space distortion and reduce the increase in beam emittance.

As the upstream RFQ and the downstream superconducting structures have typical quasiperiodicities with higher accelerating efficiency, their periodic phase advances far exceed that of the transport line. For a compact MEBT lattice design, the installation space of focusing elements, vacuum components, and the drift section for beam diagnostics is strictly restricted. To enhance the capability of beam diagnostics and the compactness of the MEBT design, the focusing structure and beam diagnostic components will be arranged alternately. Enough beam diagnostics will be installed to improve the accuracy and credibility of the system, as well as the completeness of beam information. The ac current transformers (ACCT) will be installed at both the entrance and exit of the MEBT to measure the transmission. Each focusing cell will be equipped with BPMs because the phase advance between every two adjacent cells will be over 90°. Multiple sets of profile measurement components will be available along the MEBT for transverse beam profile verification, the components include slits with Faraday cup, wire scanners, and beam scrapers. A fast Faraday cup (FFC) and bunch shape monitor (BSM) will be available for longitudinal emittance measurements. The layout of all the beam diagnostics is shown in Fig. 9.

The prevention of phase space distortions at the MEBT exit is a critical issue for the MEBT beam physics design; its importance has also been acknowledged in the design of the SNS [32], ESS [33], and ADS injector II accelerators [34]. To avoid phase space distortions in the CiADS MEBT, the positions and voltages of rf cavities were adjusted to optimize the tune depression ratio and phase advance. The resulting longitudinal phase advance of the MEBT was greater than 20°/m, whereas the tune depression was no less than 0.65. The longitudinal phase advance curve is shown in Fig. 10.

After the optimization of the longitudinal phase advance, the position of the buncher and the cavity voltage were fixed. For transverse phase advance optimization, the rms emittance growth and 99.99% emittance evolution were compared under different matching cases. And finally, with multiparticle simulation, the problem of phase space distortions was resolved. Figure 11 shows the curve of phase advance in the MEBT. The rms emittance increase in the MEBT was less than 3%, and the 99.99% emittance increase was less than 4%.

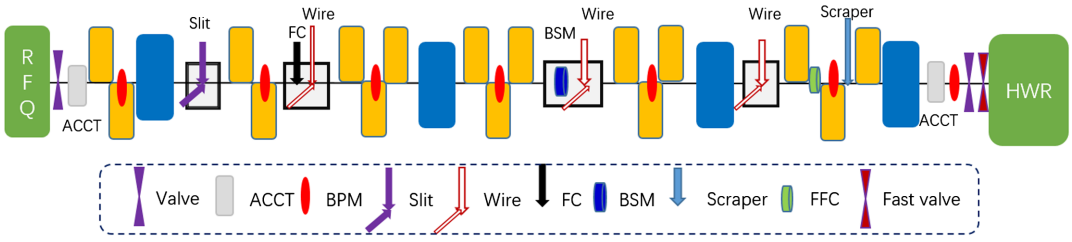

FIG. 9. Schematic layout of the MEBT.

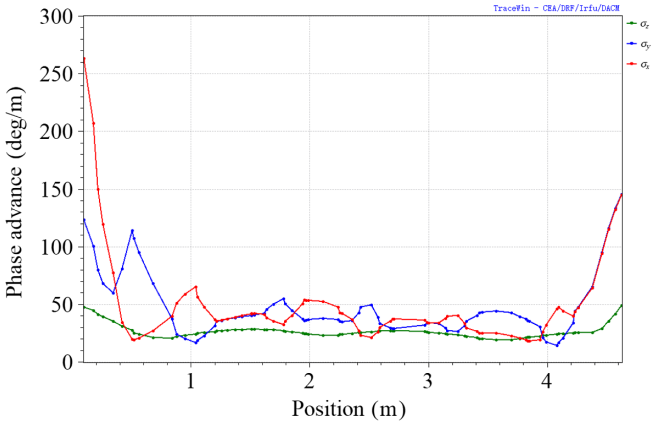

FIG. 11. The curve of phase advance at MEBT.

Based on the longitudinal and transverse phase advance analysis above, multiple particles were tracked with space-charge effect through the MEBT. Unbunched particles from the RFQ were eliminated in the MEBT to reduce the probability of beam loss in the superconducting section. Figure 12 shows the loss of untrapped particles along the MEBT with the nominal lattice. The untrapped particles are all lost in the first 1 m of the MEBT. Figure 13 shows the 4σ beam envelope with untrapped particles.

Furthermore, since the MEBT is the last room temperature section, it is the most suitable location to apply beam halo scraping. Because the beam power is as high as 10 kW in the CiADS MEBT, intercepting elements may bring serious risks when scraping the beam halo. To solve this problem, the MEBT was designed such that the cumulative phase advance was close to 360° and that the beam would evolve with a relatively smooth envelope. So, the beam pipe could be used to limit the beam halo particles at any angle within the"full" phase space. Figure 14 shows the ratio of the effective acceptance of the superconducting section to the maximum emittance of MEBT for beam pipes with different semiapertures.

The drift pipe aperture radius was optimized to be 30 mm to guarantee the minimum acceptance together with maximum transmission. The beam pipe aperture radius was

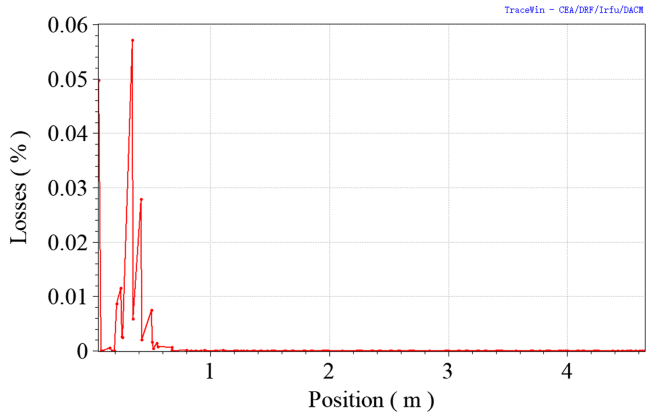

FIG. 12. Untrapped particle loss curve along the MEBT.

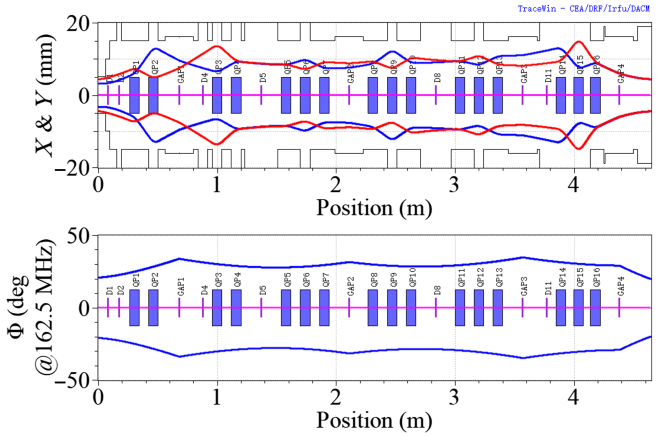

FIG. 13. Beam envelop along MEBT with space-charge effect.

about 3.75 times the rms beam envelope. The maximum emittance was less than 1.88π mm mrad at the exit of the MEBT, which was 1/9 of the effective acceptance of the superconducting section. These results indicated that the beam quality will be superior with this beam pipe dimension, and the halo particles will be far away from the boundary of the superconducting section's acceptance.

4. SC section design

Lattice structure design. The SC section was designed to accelerate a 10 mA proton beam from 2.1 to 500 MeV. The lattice design focused on achieving high acceleration efficiency and extremely low beam loss. In the SC section, the β of the proton beam changed from 0.06 to 0.76. The types of SC cavities were selected based on the energy region where they deliver the best performance. The numbers of different SC cavities, Ncell, and beta were optimized to achieve the highest acceleration efficiency.

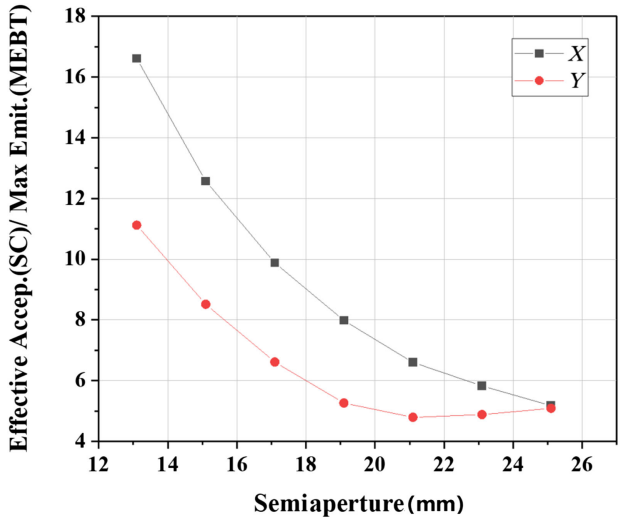

FIG. 14. Ratio of the downstream acceptance to MEBT with different semiapertures.

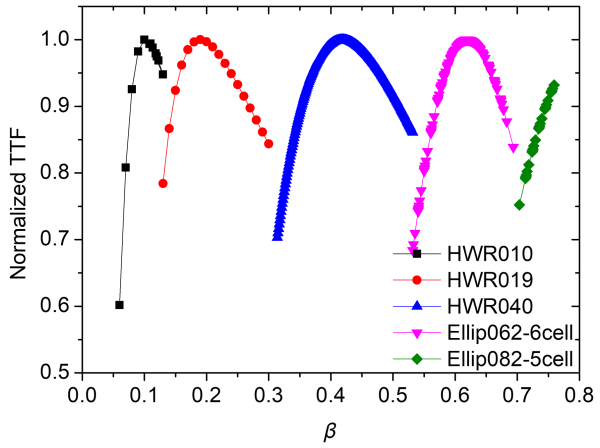

FIG. 15. Transit time factor as a function of β for the five types of cavities.

Based on the optimization, we chose five types of cavities: two 162.5 MHz half wave resonator (HWR) cavities with β_{opt} of 0.10 and 0.19, respectively, a 325 MHz HWR cavity with β_{opt} of 0.40, and two 650 MHz elliptical cavities with β_{opt} of 0.62 and 0.82, respectively. The E_{pk} (peak electric field) on the cavity's surface was limited to 30 MV/m to decrease the probability of field emission or quench; consequently, the B_{pk} (peak magnetic field) was below 60 mT for all the cavities. Additionally, power dissipation on the cavity walls was reduced by maximizing the values of the geometric shunt impedance and the geometric factor. The aperture radius of different cavities was determined according to the beam optics requirements. The main rf characteristics of the superconducting cavities are summarized in Table II. The transit time factors (TTFs) as a function of β for the five types of cavities are shown in Fig. 15 where each TTF is normalized against its maximum value.

The optics design of the SC section was optimized to operate with beam loss below 1 W/m by minimizing the emittance growth due to mismatch and space charge. The design procedure was conducted using the program TraceWin. First, we created the lattice of each SC period and set up the cavity parameters based on both the acceleration efficiency and phase advance limitation. Then, the transverse parameters were determined according to the temperature equipartition principle. Next, we performed matching, obtained beam envelopes, and conducted multiparticle simulations. Last, we performed case studies with errors and element failures. Lattice configurations of the different acceleration sections were optimized mainly based on the beam optics and low cost. Three major considerations determined the lattice design of the SC section: (i) appropriate lattice configurations to reduce beam loss probabilities from mismatch; (ii) maximized beam energy at the transition between different lattice configurations to overcome beam emittance growth from strong space charge; and (iii) minimal number of SC cavities and linac length to minimize cost of construction.

In the low energy part, the focusing period was kept short for two purposes. First, the transverse rf defocusing is proportional to the field amplitude in the cavity and its effect is largest at low velocity. Therefore, each cavity was paired with a solenoid to form a short focusing period—this enabled every cavity to fully utilize its available accelerating voltage. Second, the short focusing period can minimize the effect of the space-charge forces by limiting the drift space a beam traversed through without focusing. In order to protect the HWR cavities from potential contamination coming from the MEBT, the period in the HWR cryomodule started with an SC solenoid.

In the medium energy part and the high energy part, full period structures were chosen to minimize optics perturbations at the cryomodule-to-cryomodule transitions.

In the high-energy part, quadrupole magnets were used to increase the reliability and maintainability of this section. In addition, the effect of beam loss from the beam halo on the superconducting cavities must be taken into consideration. Quadrupoles with 80 mm beam pipe were used to scrape uncontrollable halo particles, whereas the beam pipe of elliptical cavities was 100 mm.

The cavity number and layout per period were chosen by comparing the design results with different configurations. The optimization goal was to reduce the total number of cavities without decreasing the beam performance. The lattice configuration for each section of the SC linac are shown in Fig. 16.

The optics design obeyed a number of principles. The phase advances per cell in the three-phase planes were usually kept below 90° to avoid parametric resonances and the resulting emittance growth or even halo formation [35–37]. Under the phase advance limitation, the initial φ_s at the HWR entrance was set to −40° and kept smaller than −20° degree along the whole linac to obtain enough phase acceptance and high acceleration efficiency. The transverse phase advance was determined by the equipartitioning condition lab [38]. This physical requirement and restrictions on hardware parameters determined the basic operation parameters of magnets and cavities. Figure 17 presents the synchronous phase φ_s, the corresponding accelerating field of the cavities, and the magnetic gradient of magnets. The phase acceptance was maximum at low energy and decreased with energy, thereby ramping up the acceleration efficiency.

For high-intensity accelerator physics design, the phase advance per meter needs to be kept smooth to avoid mismatch effects. Figure 18 shows the phase advance per unit length and phase advance per period.

Beam matching is a critical factor affecting beam loss in the beam dynamics design. Each section in the linac has different focusing periods, and therefore the linac is not a periodic, but a quasiperiodic structure. Transition from one focusing period to another or transition from one cryomodule to another in the beam line might lead to abrupt

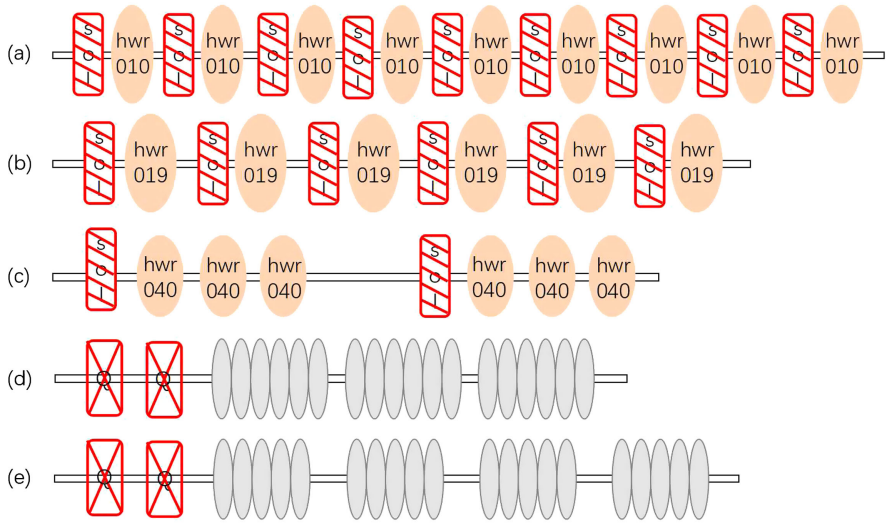

FIG. 16. The different SC cavity period layouts for the CiADS. (a), (b), and (c) correspond to the HWR sections HWR010, HWR019, and HWR040, respectively, and finally, (d) is for Ellip062, and (e) for Ellip082.

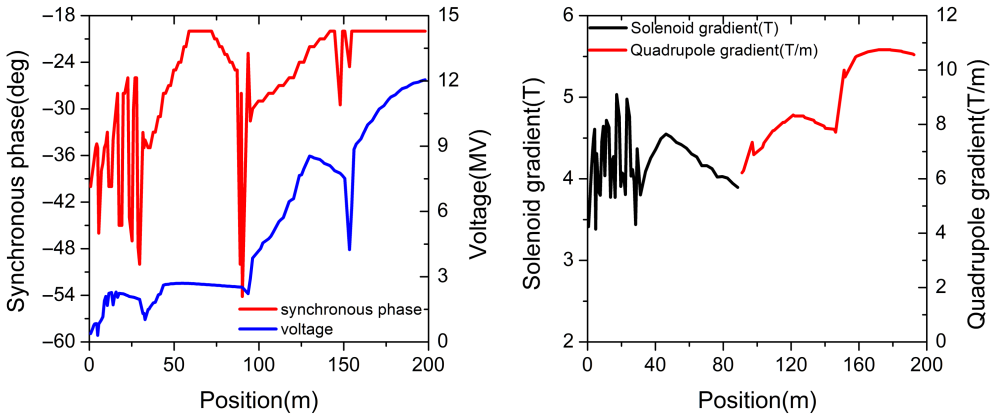

FIG. 17. Accelerating field and synchronous phase of SC cavities (left) and gradient of magnets (right).

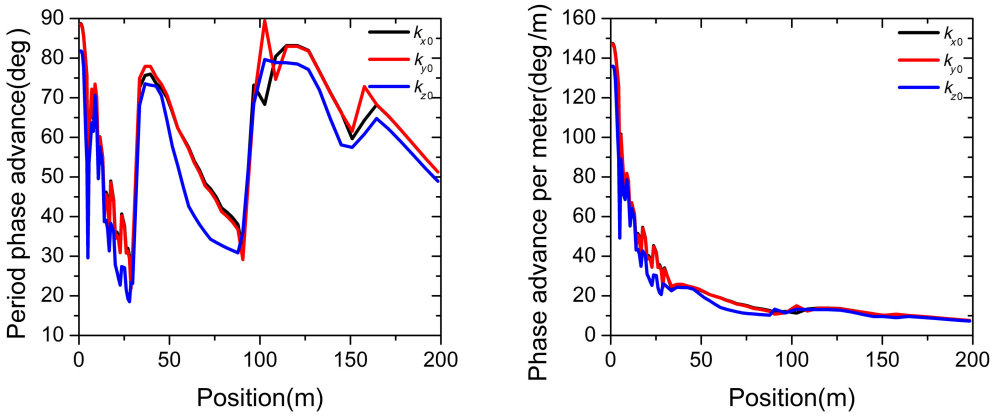

FIG. 18. Phase advance per period (left) and per unit length (right).

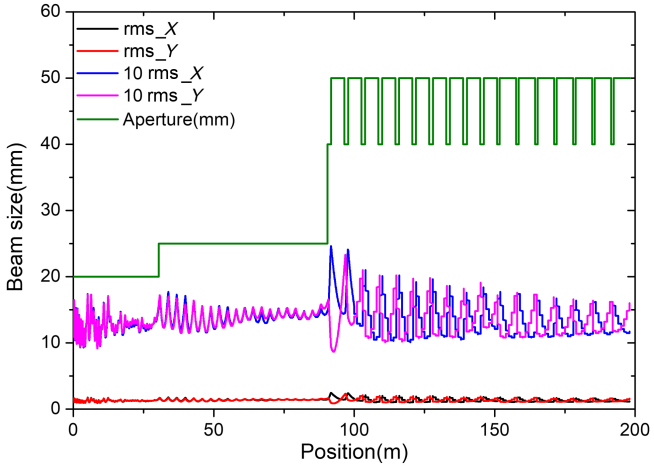

FIG. 19. Beam envelope evolution along the linac.

changes in the beam envelopes, which may result in emittance growth and halo formation. Thus, careful beam matching is required at these locations of discontinuities. The beam matching was done by adjusting the magnet gradients, cavity phases, and cavity amplitudes around the transition region in TraceWin.

In the transverse direction, the gradients of magnetic elements near the transition section were optimized with the goal of minimizing envelope oscillations. Figure 19 shows the transverse beam envelope evolution along the linac.

In the longitudinal direction, continuity of the phase acceptance at the frequency jump is a critical optimization goal. In our case, to keep the same longitudinal acceptance, the synchronous phase was generally doubled after the frequency jump. To smooth the variation of the average phase advance across the frequency jump, the accelerating gradient of the first cavity downstream was reduced. In our design, the scheme of keeping constant phase acceptance at the frequency jump, as well as smoothing the phase advance per meter, was valid. Figure 20 shows the longitudinal acceptance at the entrance of the SC section, white area, obtained by beam tracking simulations. The black area indicates the initial location of the particle that becomes lost during beam transportation. The solid blue ellipse represents the longitudinal phase space area of the distribution and contains 100% particles assumed as the input beam at the entrance of the main linac. The empty red ellipse is the maximum area of the same ellipse parameters transported through the linac without beam losses. From this, it can be said that the longitudinal acceptance contains an equivalent area of 10 times the input $\varepsilon_{\mathrm{norm},z}$.

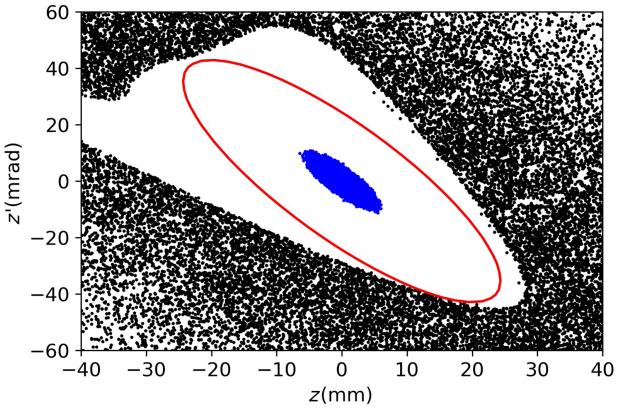

FIG. 20. Longitudinal acceptance of the SC section.

The longitudinal acceptance contained an equivalent area of 10 times the input normalized longitudinal emittance $\varepsilon_{\mathrm{norm},z}$ including 100% particles. The z corresponds to pulse length, and Fig. 21 shows the variation in the absolute value of the synchronous phase and beam phase along the linac. The synchronous phase was kept larger than 8 times the rms phase width throughout the main linac. The phase acceptance was made sufficient in the low energy section and decreased with increasing energy while the accelerating efficiency was ramped up.

Based on the design scheme, the main element parameters of the SC section are shown in Tables III and IV.

Beam dynamics simulation. Apart from the contribution from mismatch, another vital factor that can cause beam deterioration is the space-charge induced instability proposed by Hofmann [39,40]. Figure 22 shows the Hofmann chart for our design from TraceWin. Except for one point from a matching cell that fell into the region of weak resonance, all the other tune footprints were in the resonance-free region.

In order to validate the design at the full operation current, beam dynamics studies were carried out at 5 mA including space-charge effects. Multiparticle simulations were performed with the TraceWin program with 3D field-maps for cavities and magnets. An initial Gaussian beam distribution, truncated at 4σ and 5σ in transverse and

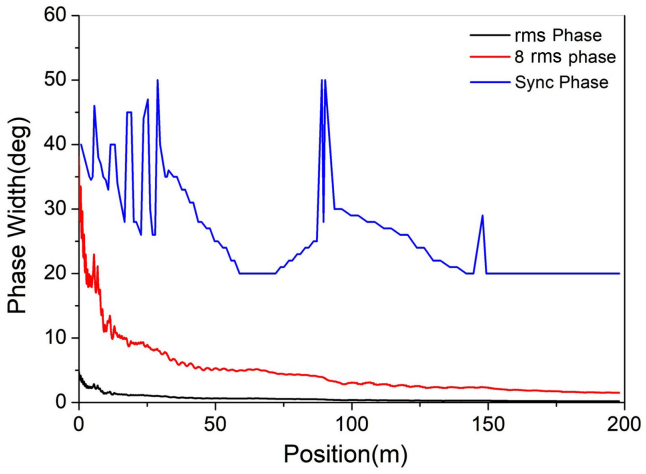

FIG. 21. Variation in beam phase and absolute synchronous phase along the linac.

TABLE III. The main cavity parameters.

	HWR010	HWR019	HWR040	Ellip062	Ellip082
Frequency	162.5	162.5	325	650	650
Aperture radius (mm)	20	20	25	50	50
E_{pk} (MV/m)	26	28	28	29	29
Eacc (MV/m)	5.42	7.27	8.46	13.69	15.87
Total number	9	24	60	30	28

TABLE IV. The main magnet parameters.

	Solenoid-1	Solenoid-2	Solenoid-3	Quadruple
Type	SC	SC	SC	NC
Aperture radius (mm)	20	20	25	40
Magnetic field (T)	6	6	6	...
Gradient (T/m)	...	...	...	16.3
Total number	9	24	20	34

longitudinal directions, respectively, was adopted. 10^5 macroparticles were used with rms normalized emittances of 0.22 (transverse) and 0.25 (longitudinal) π mm mrad based on the output beam quality of the front-end linac.

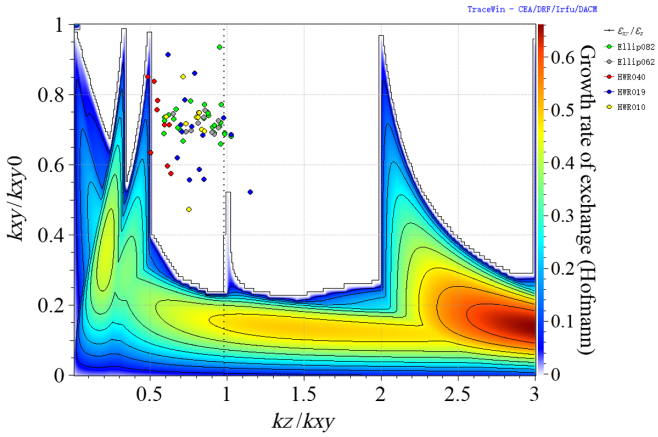

FIG. 22. Hoffman stability chart.

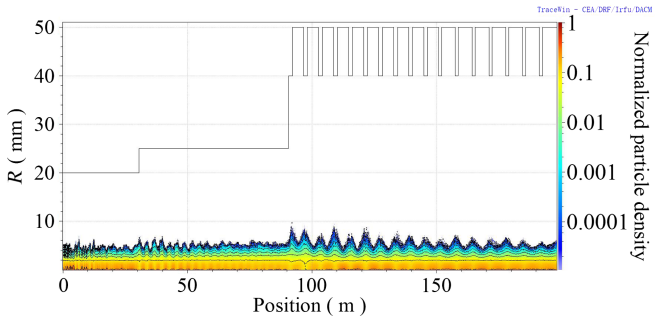

FIG. 23. Transverse beam density along the SC section. The aperture line is the physical aperture radius of the linac elements.

Some simulation results are shown below. The beam density evolutions in transverse and longitudinal along the SC section are presented in Figs. 23 and 24. Simulation results revealed that the maximum beam size was less than 1/2 of the beam pipe (see Fig. 23). The beam was stable longitudinally and there was no particle loss (see Fig. 24).

Given the importance of beam loss control, beam emittance control was the main focus of the beam dynamics studies. For multi-MW high-power linacs like CiADS, beam loss should be controlled at the level of 10^{-7}/m which renders the behaviors of halo particles highly important. Therefore, the emittance evolution for rms, 90%, 99%, 99.9%, and 99.99% fractions were studied as shown in Fig. 25. The emittance evolutions for different beam fractions were consistent, and there were no strong nonlinear behaviors in both horizontal and vertical directions. rms emittance growths were 4.4% and 2.5% in the transverse and longitudinal directions, respectively. The 99.99% emittance growths were 34.1% and 38.3% in X and Y directions and 37.7% in the longitudinal direction. There was no significant emittance and halo growth. The phase

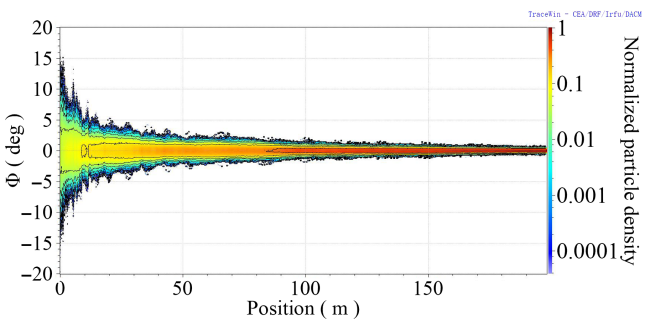

FIG. 24. Longitudinal beam density along the SC section.

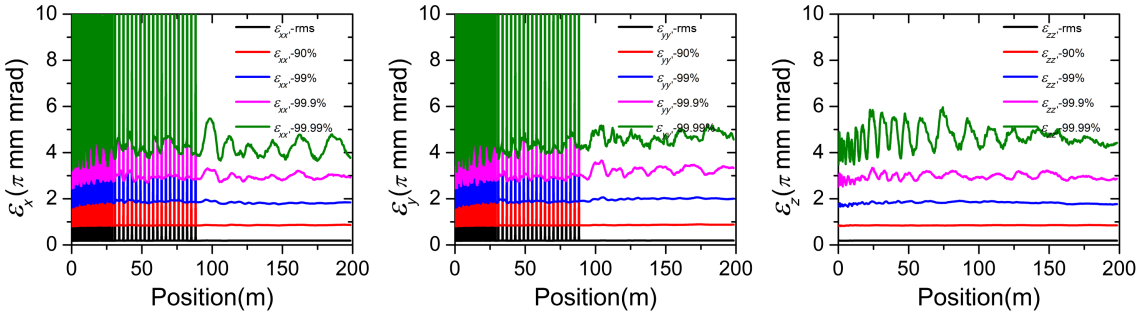

FIG. 25. Beam emittance evolution along the linac for different beam fractions.

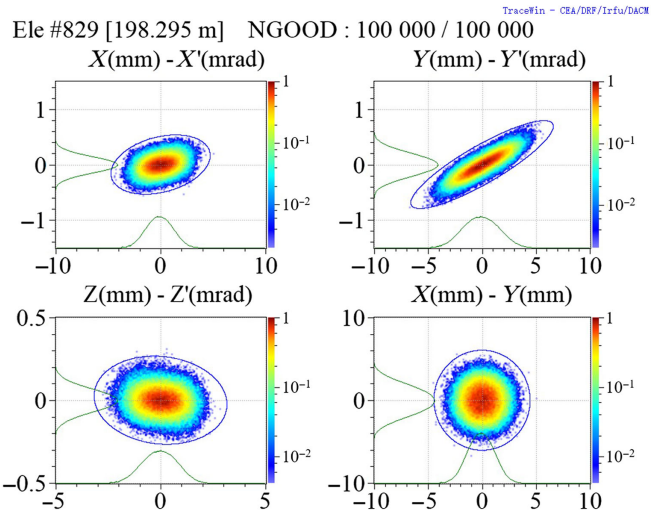

FIG. 26. Phase spaces at the exit of the SC section.

spaces at the exit of the SC section had no severe distortion as shown in Fig. 26.

5. HEBT

HEBT (high energy beam transport) includes EUS (energy upgrade segment), BLHD (beam line to high-power dump), BLR (beam line to reactor), and several other beam lines to different terminals as shown in Fig. 27. About 17 periods are reserved in EUS for the proton energy from 630 MeV to 1.4 GeV by periodic Ellip082 accelerating structure. Beam is bent to left 30° to the high-power dump with the designed power of 300 kW. 500 MeV@5 mA proton beam will be sent to the dump with a 10% duty factor.

Transverse structure periodic phase advance in EUS shifts from 60° to 30° smoothly in second order. Beam tube diameter is beyond 25 times of the beam rms size σ as shown in Fig. 28. Symmetrical achromatic design is applied via two 15° dipoles in BLHD bending section, and Fig. 29 illustrates the dispersion function. The beam is expended to the dump entrance by four quadrupoles. Beam density distribution is shown in Fig. 30.

6. End-to-end simulation

End-to-end beam dynamics simulations were performed from the ion source to the end of the linac to verify the matching between different parts. The initial particle distribution out of the ion source was assumed to be a 4D Gaussian distribution with transverse rms emittance of 0.18 mm mrad and the total particle number was 100 000.

The smooth rms envelopes along the linac shown in Fig. 31 verified the optical design and matching for the beam core along the linac. The phase space distributions at the end of the linac are shown in Fig. 32.

IV. ERROR ANALYSIS

In a high-power accelerator facility, uncontrolled beam loss poses a severe threat to the reliable and safe operation of the facility. For the CiADS linac with extremely strict requirements on beam loss, it is important to study beam performance not only in the nominal case but also in the case of errors. Error studies were conducted to evaluate the linac tolerances.

The errors mainly come in two forms: element errors and input beam errors. Element errors include translation errors, rotation errors, and field errors for all electromagnetic devices [41]. Translation errors and rotation errors are mainly caused by imperfect installation, and each error

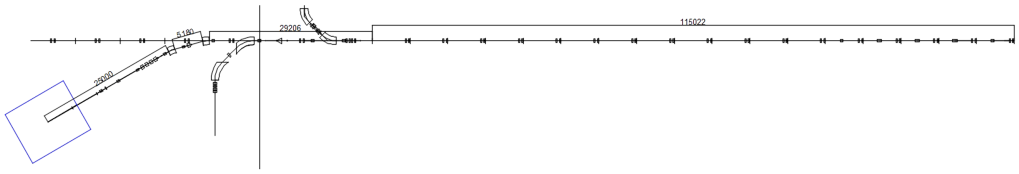

FIG. 27. CiADS HEBT layout.

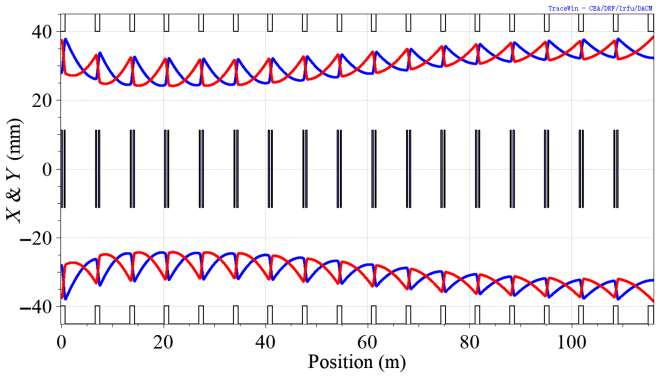

FIG. 28. Transverse 25 times rms envelope in EUS.

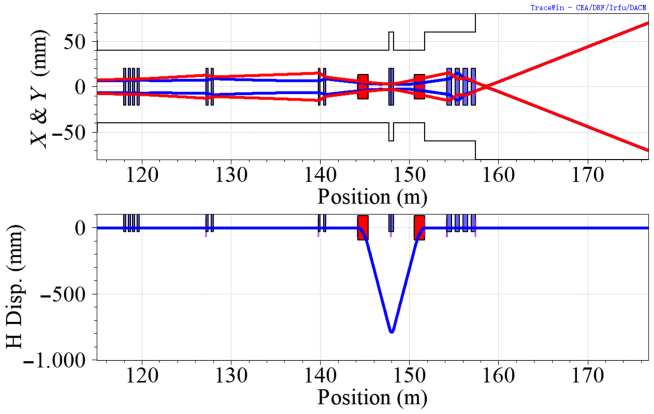

FIG. 29. Transeverse 5 times rms envelope and horizontal dispersion function in BLHD.

amplitude is distributed uniformly within plus-minus the maximum absolute error value. These errors are static and can remain constant for a long time, and they can be measured and compensated. Field errors include two components: one is gradient errors of magnetic fields from power supplies for magnet elements and another is the amplitudes and phase fluctuations from power sources for cavities. These errors are random in time and cannot be compensated; they are modeled using the Gaussian distribution. In simulations of the SC linac, the output distributions from

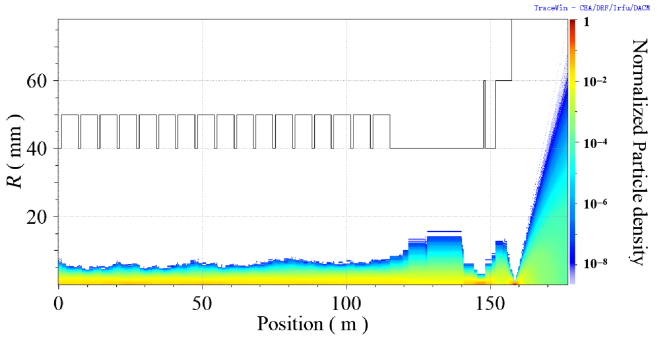

FIG. 30. Beam density from SC end to DUMP.

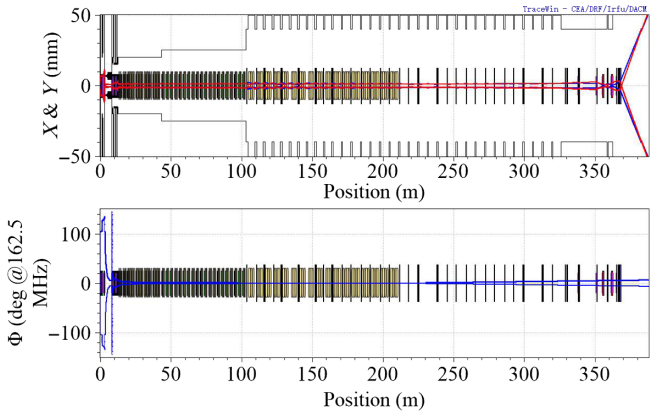

FIG. 31. rms envelope evolution from ion source to dump.

the front-end linac in TraceWin simulations were used as initial beam conditions. Input beam errors arise from possible deviations in these initial beam parameters.

The error studies were conducted in three steps. First, we independently applied each of the errors to find the boundary conditions. Second, all errors of the same type were applied simultaneously to analyze the influence of each type of error. Third, in a procedure called combined errors, all errors were applied simultaneously to verify the robustness of the physics design. Each error study consisted of 100 independent runs with a beam distribution of 1×10^5 macroparticles. We centered the error studies around two figures of merits: beam loss and normalized rms-emittance growth.

Each element error was bounded by the requirements of no beam loss and the same emittance growth as the ideal case. The initial values of these errors are summarized in Table V. The amplitudes of these errors were selected based on the beam performance of multiparticle simulations and technical feasibility.

Figure 33 shows beam envelope and beam loss evolution along the linac when all the static and dynamic element

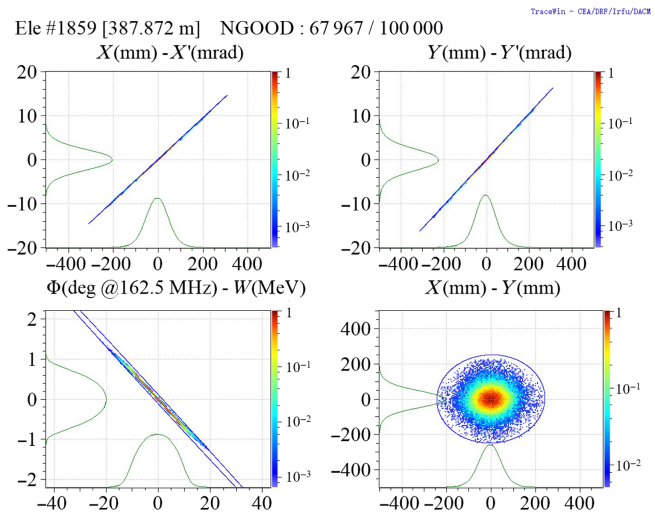

FIG. 32. The phase space distributions at the end of the linac.

TABLE V. Element error values.

		Static error		Dynamic error	
	Element	$\Delta x/\Delta y/\Delta z$ (mm)	$\Delta\phi_x/\Delta\phi_y/\Delta\phi_z$ (mrad)	Gradient of magnet (%)	Amplitude and phase of cavity (degree/%)
HWR010	Sol	0.5/0.5/1	1.4/1.4/0	0.1	
	Cav	0.5/0.5/1	7.6/7.6/0		0.1/0.1
HWR019	Sol	0.5/0.5/1	0.6/0.6/0	0.1	
	Cav	0.5/0.5/1	2.8/2.8/0		0.1/0.1
HWR040	Sol	0.5/0.5/1	0.4/0.4/0	0.1	
	Cav	0.5/0.5/1	1/1/0		0.1/0.1
Ellip062	QUAD	0.2/0.2/1	0/0/1	0.1	
	Cav	0.5/0.5/1	1/1/0		0.1/0.1
Ellip082	QUAD	0.2/0.2/1	0/0/1	0.1	
	Cav	0.5/0.5/1	0.9/0.9/0		0.1/0.1

errors were applied simultaneously. The percentage of most of the maximum beam size to beam aperture radius was larger than 90%, and there was a high probability of beam loss, and beam loss less than 1 W occurs at the transition section of 30 m. Doubling the error amplitudes in Table V presented a large transverse offset that resulted in beam loss, as is shown in Fig. 34. The envelopes reached the aperture radius in the HWR section, and noticeable power

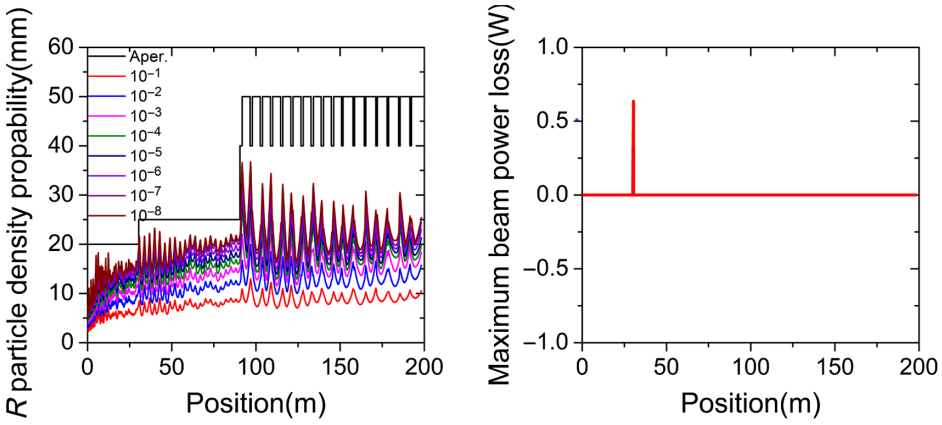

FIG. 33. Transverse beam size (left) and beam power loss (right) along the linac when all element errors were applied simultaneously as presented in Table V.

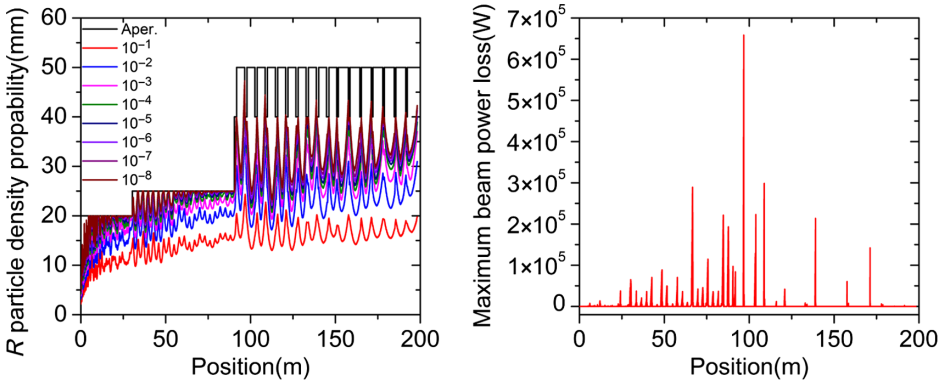

FIG. 34. Transverse beam size (left) and beam power loss (right) along the linac when double the element errors presented in Table V were applied simultaneously.

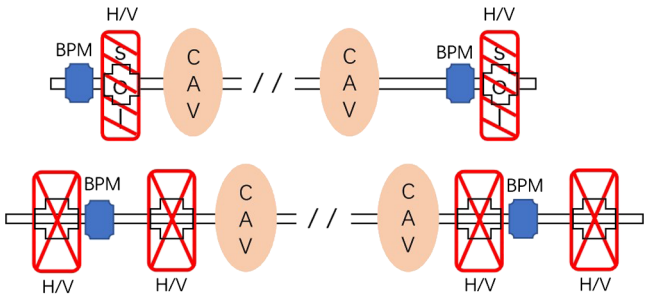

FIG. 35. Layout of orbit correction scheme.

loss was recorded, mainly in the transition section of two cryomodules in the low energy part.

It is important to perform beam centering during beam commissioning and beam operation. The beam centroid offset from static errors can be corrected based on the beam alignment method. Based on the lattice design, we devised a correction scheme for the CiADS superconducting acceleration section which employed a pair of corrector and BPM in each focusing period, as shown in Fig. 35. In the low energy part, a BPM and a solenoid with steering coils formed a compact period. In the high-energy part, the correction scheme combined a BPM and a quadrupole doublet with integrated steering coils. The BPMs were simulated with an accuracy of ± 200 μm to consider their displacements and measurement resolution. On one hand, this scheme ensured good sensitivity without damaging the periodicity of the structure. On the other hand, considering the BPM is easy to break, this solution was highly fault tolerant. An error analysis was carried out to verify the tolerance of the basic design and the degradation in beam properties was estimated with or without corrections using the TraceWin program. The effectiveness of the correction scheme was demonstrated by applying the combined element errors. The maximum beam size was above 10 mm in the transverse plane and 1.8° in the longitudinal plane as shown in Fig. 36. Applied correction reduced the transverse residual orbit error from 6 to 0.6 mm along the linac as shown in Fig. 37. The maximum steering strength in the corrector was below 5.4×10^{-3} Tm as presented in Fig. 38.

Errors in input beam parameters are another factor influencing beam quality. Such errors include the input beam displacement and rotation errors, Twiss parameters mismatch, emittance errors, beam current error, phase error, energy error, and so on. The beam current error, phase error, and energy error were found to have little impact on the beam within their possible values. So, we focused on the input beam displacement and rotation errors, beam emittance errors, and Twiss parameters mismatch errors. Table VI presents the input beam error amplitudes.

Figure 39 shows the emittance growth compared with the ideal machine case at the error settings presented in Table VI. For the combined case, the emittance growth was about 3% in the longitudinal direction and 12% in the transverse direction, and there was no beam loss. Compared with element errors, input beam errors had a limited impact on the beam performance. The envelope evolution is shown in Fig. 40.

Finally, we applied all element errors and input beam errors to carry out a comprehensive simulation to verify the robustness. In the ideal machine case, unwanted beam losses did not occur and the normalized rms emittance growth was less than 40%. When element errors and input beam errors were applied without any correction, the beam loss rate exceeded the safety limit of beam operation. When the one-by-one correction scheme was implemented, beam performance was restored and approached that of the ideal machine. Figure 41 presents the maximum envelopes for the ideal machine and error cases with correction. Given applied corrections, the envelopes behaved similarly to those of the ideal machine. There was no beam loss along the linac, and the rms energy deviation was less than

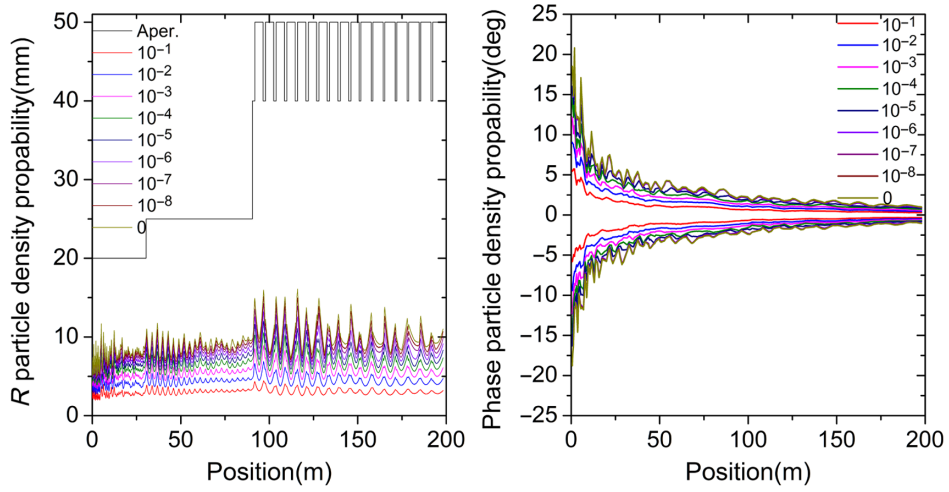

FIG. 36. Beam size with correction in the transverse and longitudinal planes along the linac.

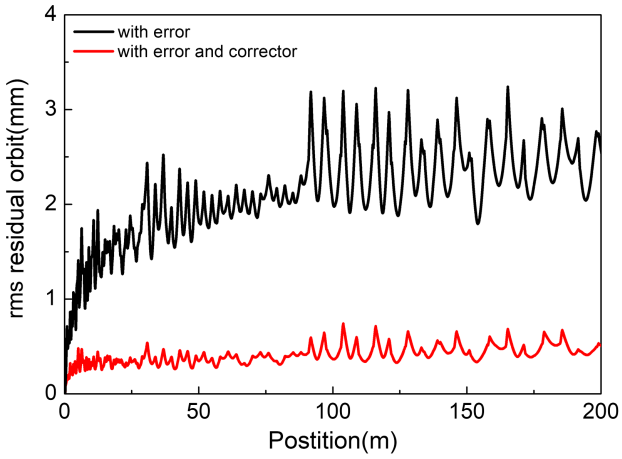

FIG. 37. Transverse residual orbit in the transverse plane along the linac.

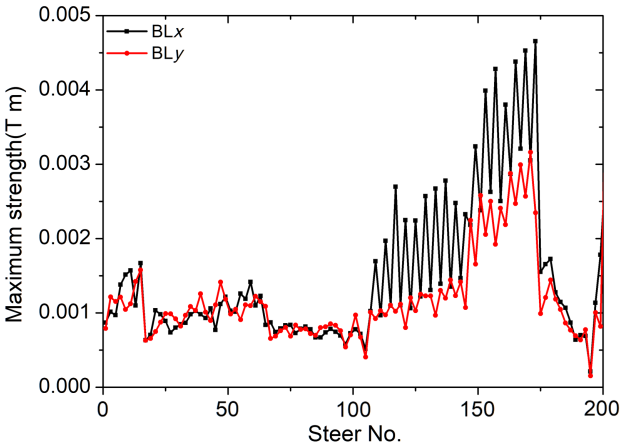

FIG. 38. Maximum steering strength in the corrector along the linac.

TABLE VI. Input beam errors.

Description	Error amplitude
$\Delta x, \Delta y$ (mm)	0.5
$\Delta x', \Delta y'$ (mrad)	0.5
ΔI (mA)	0.1
$\Delta\varphi$ (deg)	1
Emittance growth—$x/y/z(\%)$	10
Mismatch—$x/y/z(\%)$	5

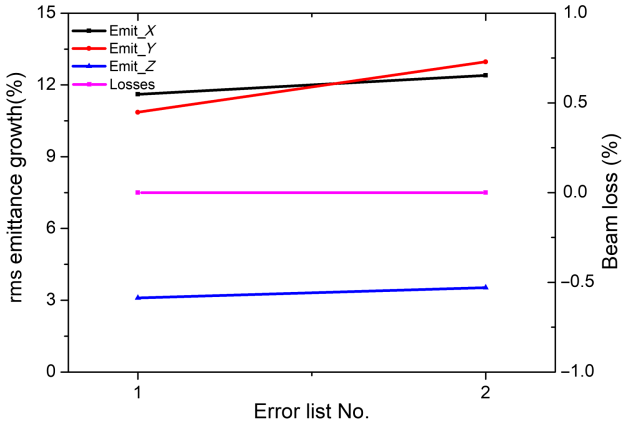

FIG. 39. Emittance growth compared with the ideal machine case at the error settings presented in Table VI.

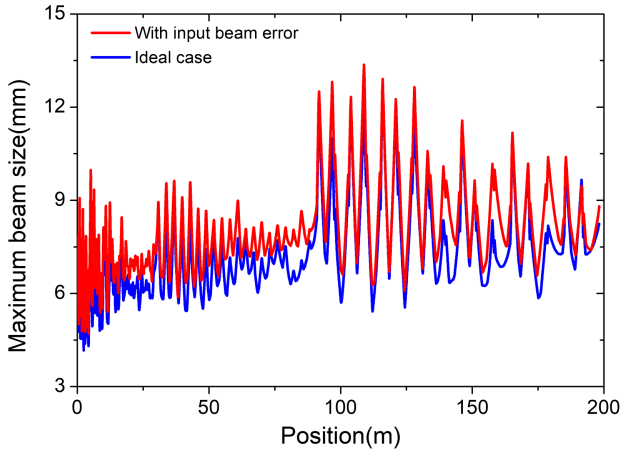

FIG. 40. Maximum beam size with and without input beam errors presented in Table VI.

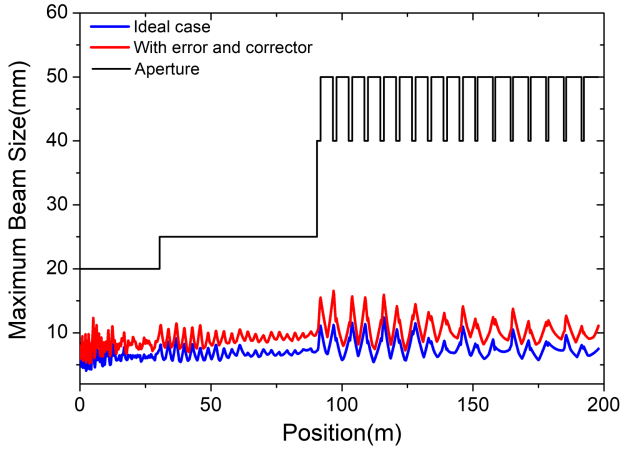

FIG. 41. Transverse beam density for the ideal machine and error cases with orbit correction.

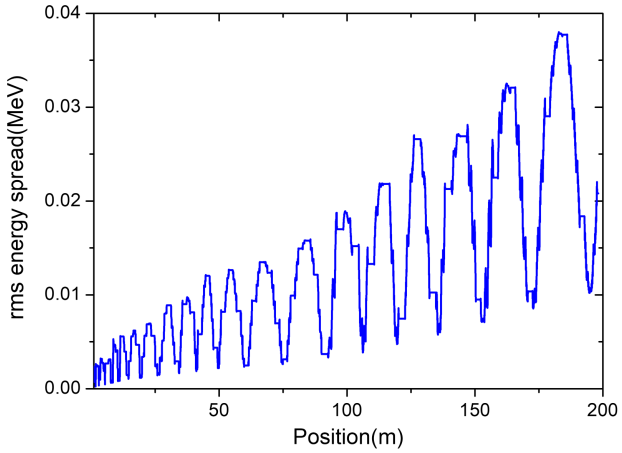

FIG. 42. rms energy deviation along the linac.

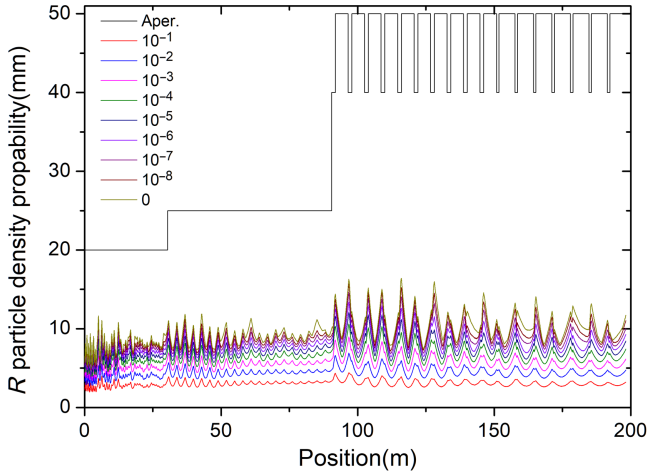

FIG. 43. Transverse beam density with errors and orbit correction.

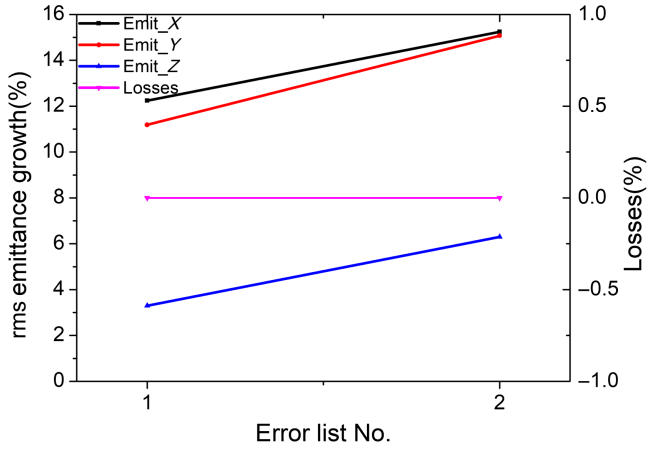

FIG. 44. Transverse and longitudinal normalized rms emittance evolution.

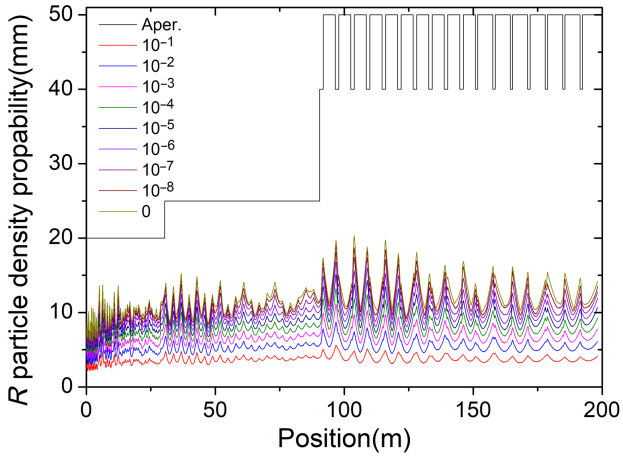

FIG. 45. Transverse beam density along the linac with double errors and orbit correction.

0.04 MeV as shown in Fig. 42. The simulation results demonstrated that the correction scheme is important to beam operation when errors exist.

Figure 43 shows the transverse beam density with errors and corrections. The envelope evolution was smooth even for the halo particles. The beam was under control and there were relatively big margins in the transverse planes. The normalized rms emittance growths were less than 4% and 12% in the longitudinal and transverse directions, respectively, with errors and corrections, as shown in Fig. 44. Doubled errors were applied to verify the sensitivity of the beam to the errors. Beam envelopes with different proportions of outlying particles are presented in Fig. 45.

Figure 45 shows the beam density along the linac with double errors. The maximum beam size was less than the aperture radius size, and there was no beam loss along the whole linac. Table VII lists the rms emittance growth with or without errors. It can be seen that there was about an additional 16% average emittance growth in the transverse and longitudinal planes with double errors. No beam loss was observed. The normalized rms emittance was also nearly the same as the results at standard errors, which means that it was still in the linear region. All the simulation results indicated that the baseline physics design has high tolerance.

TABLE VII. rms emittance growth with or without errors@double errors.

	rms emittance growth_X (%)	rms emittance growth_Y (%)	rms emittance growth_Z (%)	Beam loss (%)
EI	12.7	11.6	3.6	0
2*EI	14.8	14.5	3.6	0

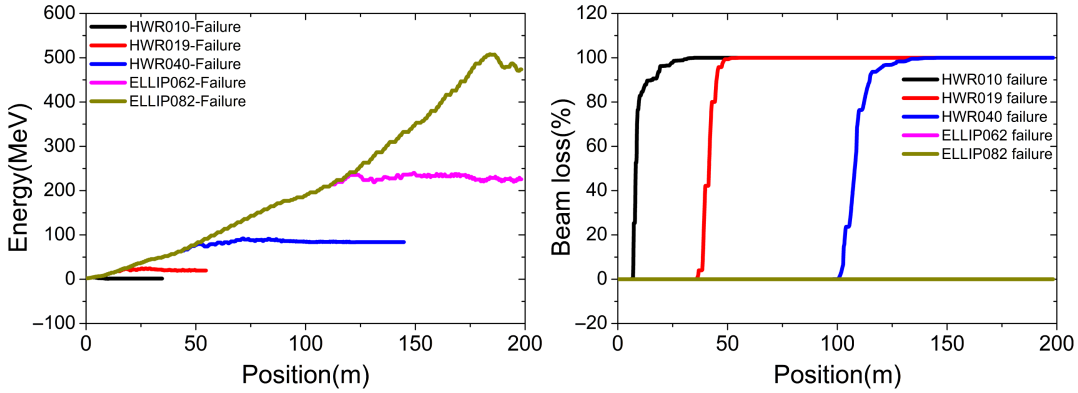

FIG. 46. Energy evolution (left) and beam loss (right) @ cavity failure in each acceleration segment of CiADS linac.

V. FAILURE COMPENSATION AND REMATCH SCHEME

High reliability, as characterized by the different numbers of beam trips, is the most crucial requirement for an ADS accelerator. Besides conservative operation of all hardwares and redundancy by design, quick online compensation in the case of device failure is an effective way to increase reliability.

Magnet failures and cavity failures are two types of element failure situations which will induce serious beam loss along the accelerator. Compared with magnet failure compensation, cavity failure compensation is more complex. For cavity failures, in addition to Twiss parameters matching, energy compensation is another critical matching target. Not only will it decrease the final beam energy, failure to achieve energy compensation will also cause beam loss in part of or the entire downstream linac.The phase slip caused by velocity change is the main reason which makes the beam go out of the acceptance of the downstream acceleration section. The energy evolution and beam loss when one cavity failure occurs in each acceleration segment of the CiADS linac are shown in Fig. 46.

Global compensation and local compensation [42–44] are the two traditional methods that are widely used to compensate for cavity failure. Their schematics are shown in Fig. 47. The global compensation method uses all the components downstream of the failed cavity to achieve

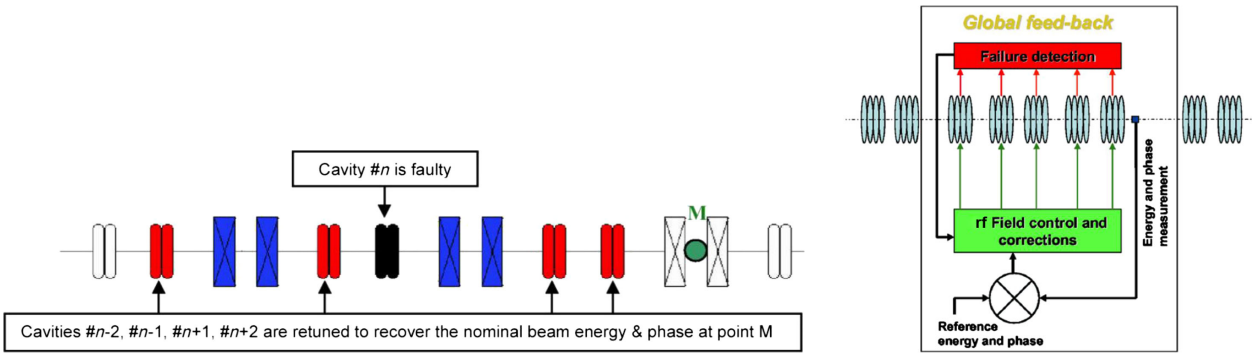

(a). Local compensation (b). Global compensation

FIG. 47. Principles of local (a) and global (b) compensation method [42].

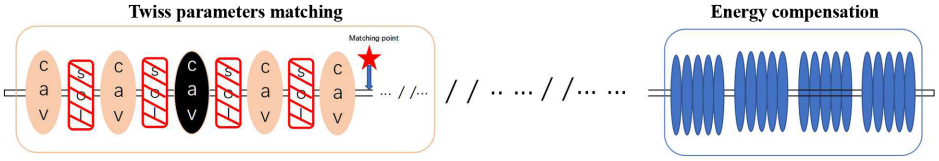

FIG. 48. Principle of piecewise compensation method.

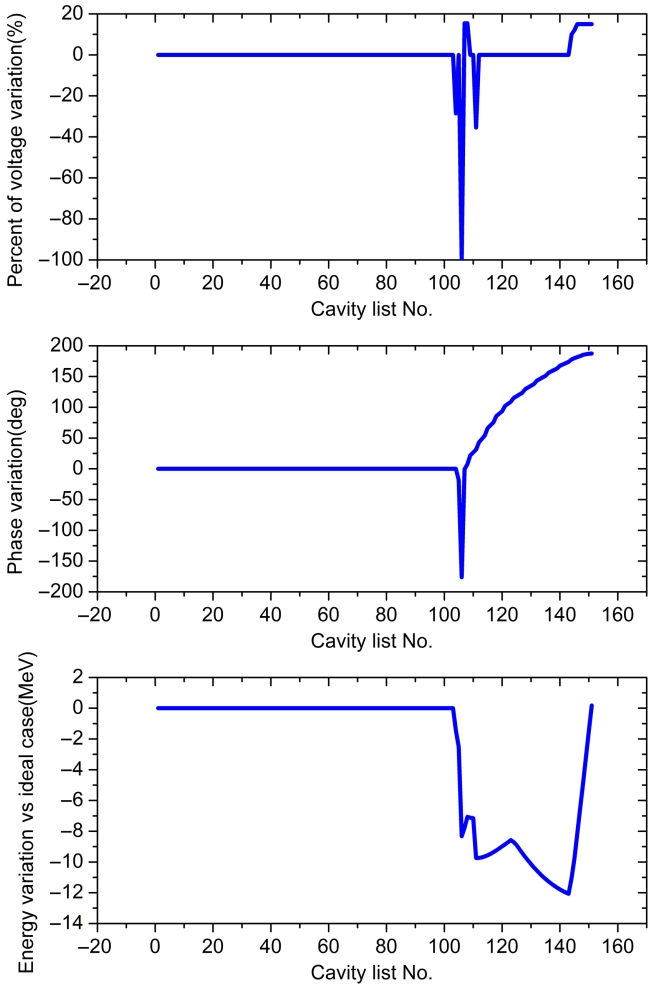

FIG. 49. Compensation process of Ellip062 cavity failure situation.

compensation and rematch. One example of its application is the SNS accelerator [45]. The lattice parameters are redesigned based on the condition of cavity failure in this scheme, and the adjustment is particularly complex. In comparison with global compensation which may involve elements far downstream of the failed element, local compensation only adjusts the several elements adjacent to the failed element to recover design beam properties at a rematch point shortly downstream. Local compensation is usually possible because the nominal operation voltages for the cavities leave about 30% redundancy, but it is difficult to apply in the very low-energy part where compensation ability is more limited [45].

Based on the characteristics of global compensation and local compensation mentioned above, combined with the physical characteristics of the CiADS linac, we proposed a novel compensation method for cavity failure which we named as piecewise compensation method [46]. This compensation method is a hybrid approach between global and local compensation for cavity failure. Unlike global compensation, this approach separates beam Twiss parameter matching and energy compensation based on the characteristics of beam transmission and the compensation capabilities of cavities. The principle is presented in Fig. 48. It achieved Twiss parameters rematch and energy compensation separately for cavity failure based on the characteristics of the CiADS linac. First, we focused on Twiss parameters rematch to avoid beam loss at the location where the failure occurred, and this process was achieved by adjusting the neighboring cavities and magnets of the failure cavity. Second, the acceleration capability of the high beta cavity is much greater than that of the low beta cavity, and it is more effective to achieve energy compensation by cavities in the high energy part. So, we used the cavities of the last three cryomodules to achieve energy compensation. The energy that is compensated is distributed to all the cavities of the last two cryomodules, and minimal voltage redundancy is taking as the optimal target. This method can greatly reduce the gradient redundancies of cavities. We present below the simulation results of superconducting cavity failures based on the piecewise compensation method in the CiADS superconducting linac.

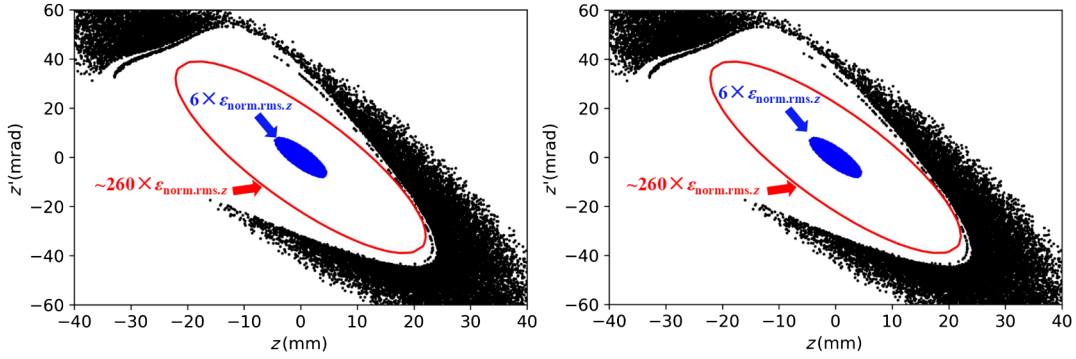

FIG. 50. Longitudinal acceptance at the entrance of the SC section for one Ellip062 cavity failure situation. Left: piecewise compensation method, Right: local compensation method.

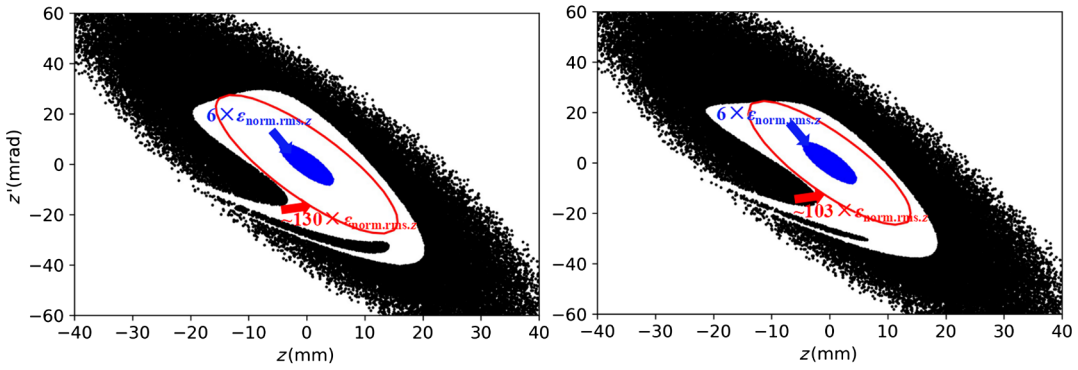

FIG. 51. Longitudinal acceptance at the entrance of the SC section for one HWR010 cavity failure situation. Left: piecewise compensation method, Right: local compensation method.

Taking the compensation of single Ellip062 SRF cavity failures as an example to explain the piecewise compensation method. As it was explained above, the rematching is accomplished by adjusting E_{acc} and ϕ of the nonfaulty element, and energy recovery was accomplished by adjusting E_{acc} of cavities in the high energy section. Figure 49 presents variation of E_{acc}, ϕ, and the beam energy for the compensation of the SRF cavity 106 in the Ellip062 section, as an example. In this case, the scheme comprises five SRF cavities for rematching Twiss parameters: two upstream and three downstream. The failure was simulated by setting the values of the faulty-SRF cavity to zero, as shown in the top plots of Fig. 49. The bottom figure of Fig. 49 presents an increase in the beam energy of the compensation scheme. The beam energy is recovered at the end of the SC section by increasing the E_{acc} of the cavities in the last two cryomodules. During compensation, the variation of the rf phase can be got from below equation:

$$\Delta\phi_{\mathrm{rf}} = \Delta\phi_{input} + \Delta\phi_{abs} \tag{1}$$

$\Delta\phi_{\mathrm{rf}}$ is the change in each cavity's phase setpoint, $\Delta\phi_{\mathrm{input}}$ is the change in the phase slip through the cavity because the beam energy has changed from the nominal case, and $\Delta\phi_{\mathrm{abs}}$ is the change of absolute beam cumulative phase. The variation of the rf phase can be obtained through the variation of phase slip and absolute phase.The middle figure of Fig. 49 presents the variation of the rf phase of the cavity.

The readjusted values had a significant impact on the longitudinal acceptance. Figure 50 presents acceptance for the situation of one Ellip062 cavity failure. Compared with the local compensation scheme, the piecewise compensation method has the same acceptance. However, in the low energy section, the effect on the acceptance is different with the local compensation scheme and piecewise compensation when a cavity fault. As shown in Fig. 51, the ratio of acceptance to the input emittance is larger than 26% with piecewise compensation scheme than that with local compensation scheme. So, the piecewise compensation scheme has a greater advantage in keeping large acceptance.

The superconducting (SC) section of the CiADS linac is divided into HWR010, HWR019, HWR040, Ellip062, and Ellip082 based on SC cavity types. Figures 52–54 show the compensation results of different failure situations in the case of one cavity failure in each segment. After applying the piecewise compensation method, the increase of beam size was less than 5% at the rematch location except the case of HWR010 failure compensation. Multiparicle simulations showed that less than 13% growth in the rms emittances and about 67% growth in the 99.99% emittance occurred after applying the piecewise compensation method. The envelope and emittance evolutions after compensation indicated that a good matching was achieved, and the process was achieved by adjusting the neighboring cavities and magnets of the failed cavity. Figure 54 presents the variation in cavity voltage, absolute phase, and energy gain after compensation compared with the ideal case. After compensation, the final energy was the same as the ideal case, and the operating reserve requirement of the cavity field only needs to be imposed upon the last type of cavities. This compensation scheme achieved Twiss parameters rematching and energy compensation, and the adjustment of cavity voltage was less than 10% under the condition of one cavity failure. In addition, the fact that compensation can be achieved when the energy is less than 10 MeV enabled the piecewise compensation method to replace the two parallel injectors compensation scheme in the very low energy part.

Cavity failure can result in degraded longitudinal beam quality and even beam loss due to insufficient longitudinal focusing over long distances. The occurrence of cavity failures in the transition section has the greatest impact on the low energy part. Figures 55 and 56 present the compensation results of one cavity failure at the

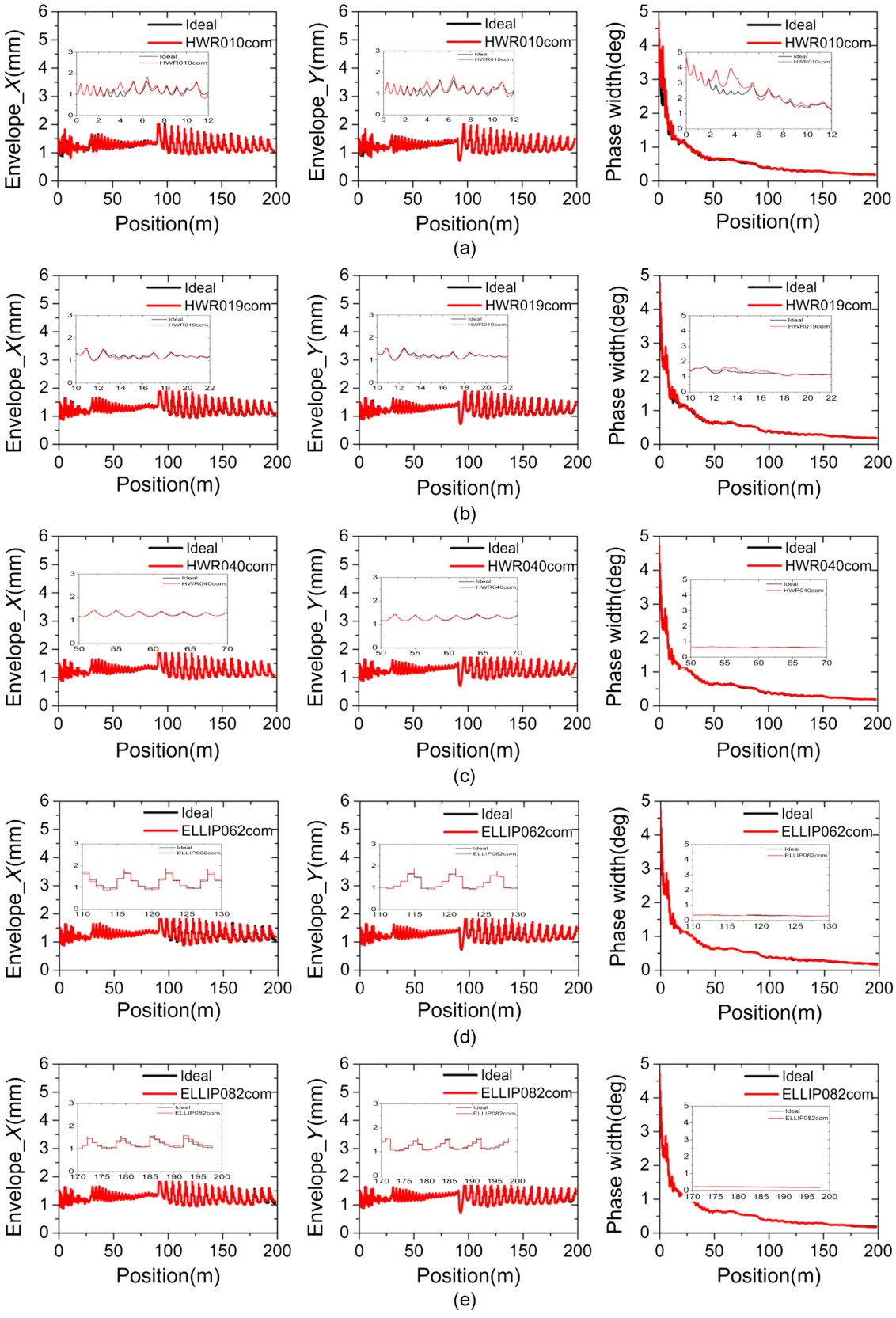

FIG. 52. Envelope evolution of different failure situations in each section. (a) Failure @ HWR010 section. (b) Failure @ HWR019 section. (c) Failure @ HWR040 section. (d) Failure @ Ellip062 section. (e) Failure @ Ellip082 section.

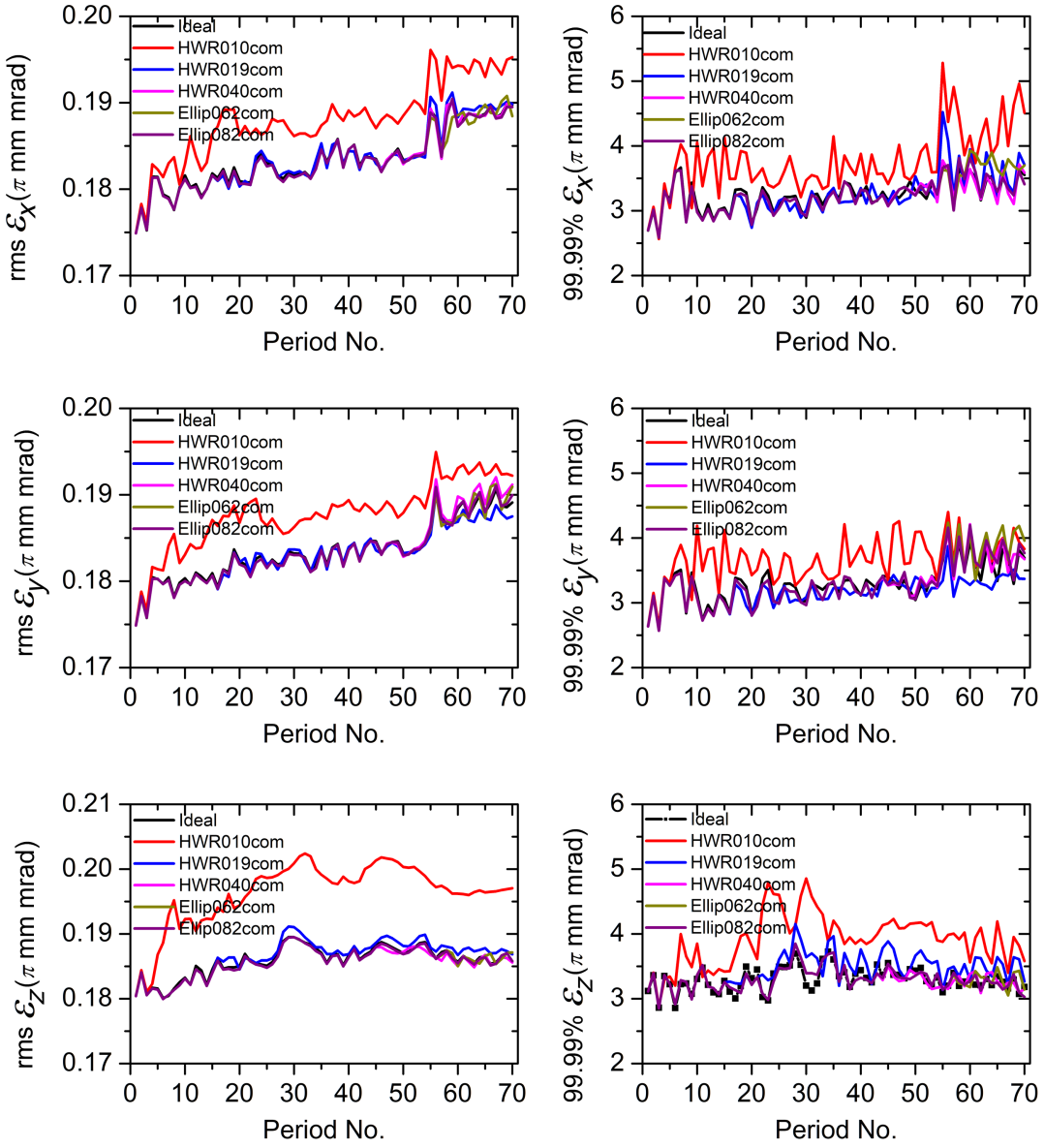

FIG. 53. rms (left) and 99.99% (right) emittance evolution of different failure situation in each section.

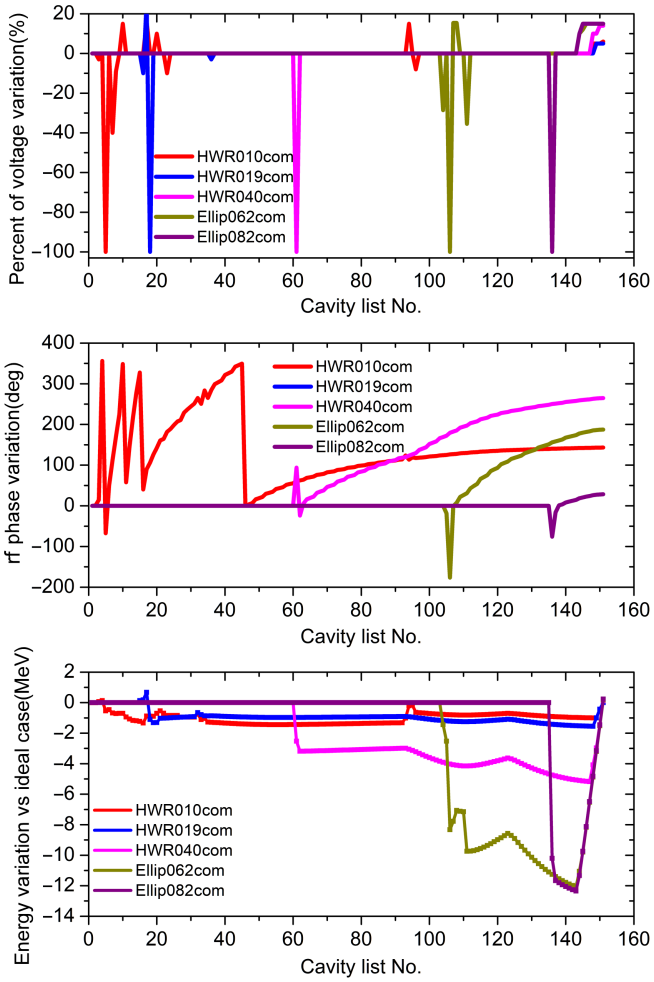

FIG. 54. Compensation process of different failure situations in each section.

transition between HWR010 and HWR019. The envelope evolution after compensation indicated that a good matching was achieved. The rms emittance growth is less than 15% and about 80% growth in the 99.99% emittance occurred after failure compensation. The beam quality is controllable.

VI. CONCLUSIONS

The physics design of the CiADS linac was carried out based on state-of-the-art technologies in high-power proton linacs. The design work was in the phase of engineering design. The linac beam dynamics simulation was presented in the ideal case. Beam losses were not recorded due to the large beam acceptance, the rms emittance growth was lower than 5% in the transverse plane and 3% in the longitudinal plane, and the 99.99% emittance growth was lower than 40% in the three planes.

Error studies were conducted to validate the robustness of the physics design in controlling beam loss and emittance growth given realistic error values. The one-to-one correction scheme demonstrated its ability to restore the transverse beam centroid. In addition, it controlled the emittance growth and the beam envelopes. Thus, it is mandatory to have a correction scheme for the CiADS linac. In the CiADS linac beam dynamics simulation, applied corrections could achieve zero beam loss even when all standard errors (element errors and input parameter errors) were present.

Piecewise compensation method is proposed and applied to CiADS linac for extremely strict control on beam-loss level by controlling emittance growth. Simulation results indicate that the beam loss is controllable.

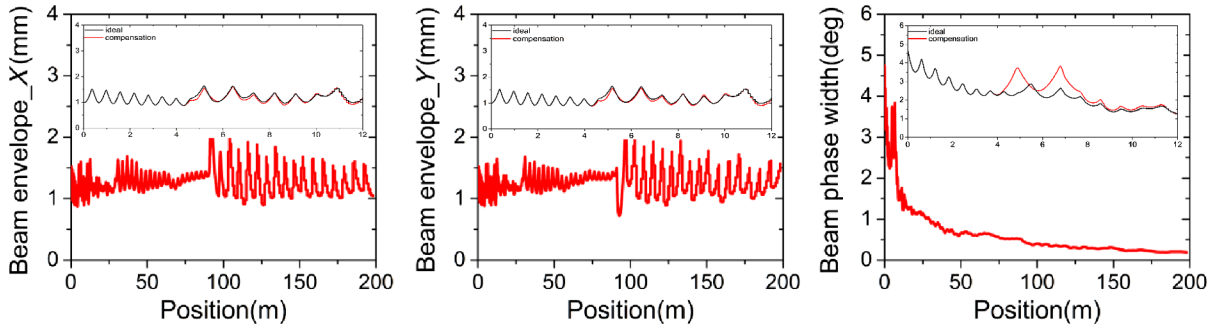

FIG. 55. Envelope evolution of one failure situation at the transition between HWR010 and HWR019.

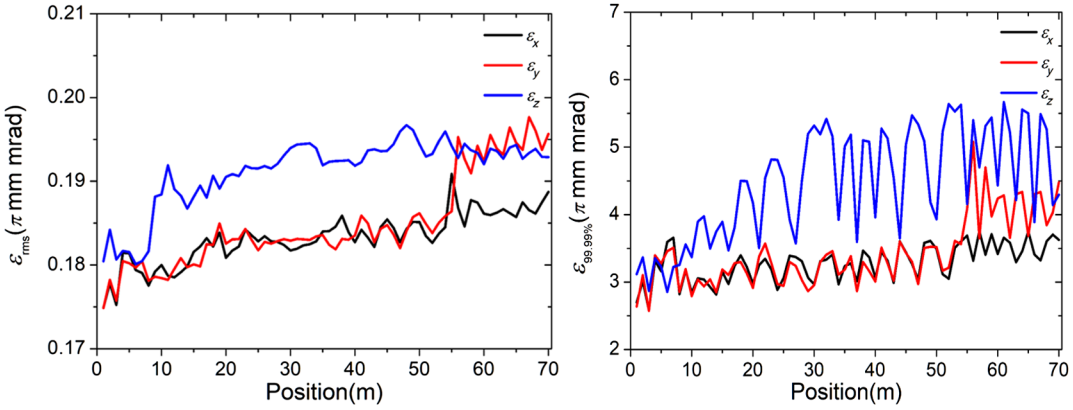

FIG. 56. rms (left) and 99.99% (right) emittance evolution of one failure situation at the transition between HWR010 and HWR019.

ACKNOWLEDGMENTS

The authors would like to express their sincere acknowledgment to the colleagues in the CiADS accelerator team and especially the beam dynamics group for their comments, suggestions, and discussions. The work is supported by the Large Research Infrastructures China initiative Accelerator Driven System (2017-000052-75-01-000590), the Natural Science Foundation of China (Grant No. 11525523), and NSAF (Grant No. U1730122).

[1] H. At Abderrahimh, J. Galambosd, Y. Gohara *et al.*, Accelerator and target technology for accelerator driven transmutation and energy production, Technical Report No. FERMILAB-FN-0907-DI, LA-UR-10-06754, 2010, https://doi.org/10.2172/1847382

[2] F. Carminati, C. Rubbia *et al.*, An energy amplifier for cleaner and inexhaustible nuclear energy production driven by a particle beam accelerator, CERN Report No. CERN/AT/93-47(ET), 1993.

[3] Jun-shen Guo, Accelerator driven transmutation and its application (in Chinese), Nucl. Phys. Rev. **16**, 267 (1999).

[4] Wen-long Zhan and Hushan Xu, The advanced nuclear fission energy in future—ADS transmutation system (in Chinese), Bull. Chin. Acad. Sci. **3**, 375 (2012).

[5] X. U. Hushan, Yuan He *et al.*, China's accelerator driven sub-critical system (ADS) program, AAPPS **25**, 30 (2015).

[6] Shu-Hui Liu, Zhi-Jun Wang, Yue Tao *et al.*, Physics design of the superconducting section of the CiADS linac, Int. J. Mod. Phys. A **34**, 1950178 (2019).

[7] P. N. Ostroumov, Physics design of the 8 GeV H-Minus linac, New J. Phys. **8**, 281 (2006).

[8] A. Saini, V. Lebedev, J. F. Ostiguy *et al.*, Design of superconducting CW linac for PIP-II, in *Proceedings of the 6th International Particle Accelerator Conference, Richmond, VA* (JACoW, Geneva, Switzerland, 2015), MOPMA014.

[9] J.-L. Biarrotte, Design of the MYRRHA 17-600 MeV superconducting LINAC, in *Proceedings of 16th International Conference on RF Superconductivity, SRF2013, Paris, France* (JACoW, Geneva, Switzerland, 2013), pp. 129–132.

[10] P. A. P. Nghiem, N. Chauvin, O. Delferriere *et al.*, THE IFMIF-EVEDA challenges and their treatment, in *Proceedings of 46th ICFA Advanced Beam Dynamics Workshop on High-Intensity and High-Brightness Hadron Beams, HB2010, Morschach, Switzerland, 2010* (Ref. [1]), pp. 309–313.

[11] W. Hartung *et al.*, Status report on multi-cell superconducting cavity development for medium-velocity beams, in *Proceedings of the 20th Particle Accelerator Conference, Portland, OR, 2003* (IEEE, New York, 2003), pp. 1362–1364.

[12] K. Saito, N. Bultman, E. Burkhardt *et al.*, Superconducting rf development for FRIB at MSU, in *Proceedings of 27th International Linear Accelerator Conference, LINAC2014, Geneva, Switzerland* (JACoW, Geneva, Switzerland, 2014), THIOA02.

[13] P. Michelato, A. Bellandi, M. Bertucci *et al.*, ESS medium and high beta cavity prototypes, in *Proceedings of the 7th International Particle Accelerator Conference, IPAC-2016, Busan, Korea* (JACoW, Geneva, Switzerland, 2016), WEPMB011.

[14] C M. Piaszczyk, Operational experiences at existing accelerator facilities, in *Proceedings of the Workshop on Utilisation and Reliability of High Power Proton Accelerators, Mito, Japan* (1999), p. 446.

[15] Stuart Henderson, Accelerator systems overview and plans, Accelerator Advisory Committee (2010).

[16] Glen D. Johns, Operations report for FY12 and FY13-Q1/2, Accelerator Advisory Committee (2013).

[17] Yuan He, Teng Tan, Andong Wu *et al.*, Operation experience at CAFe, in *Proceedings of the 20th International Conference on RF Superconductivity, East Lansing, MI* (JACoW, Geneva, Switzerland, 2021).

[18] Jiaosai Li, Youxin Chen, Jing Wang, Feng *et al.*, Beam fast recovery study and application for CAFe, in *Proceedings of the 18th International Conference on Accelerator and Large Experimental Physics Control Systems, ICALEPCS2021, Shanghai, China* (JACoW, Geneva, Switzerland, 2021), 10.18429/JACoW-ICALEPCS2021-WEPV01.

[19] M. Eshraqi, H. Danared, and R. Miyamoto, Beam dynamics of the ESS superconducting linac, in *Proceedings of HB2012, Beijing, China* (2012), TUO3B02.

[20] A. Shishlo, Beam dynamics issues in the SNS LINAC, in *Proceedings of the 24th Particle Accelerator Conference, PAC-2011, New York* (IEEE, New York, 2011), MOOBS1.

[21] M. Eshraqi, M. Brandin, C. Carlile *et al.*, Beam dynamics and design of the ESS LINAC, in *Proceedings of HB2010, Morschach, Switzerland* (2010), TUO1B01.

[22] N. Chauvin, A. Mosnier, P. A. P. Nghiem *et al.*, Beam dynamics simulation of Superconducting HWR option for the IFMIF LINAC, in *Proceedings of the 11th European Particle Accelerator Conference, Genoa, Italy, 2008* (EPSAG, Geneva, 2008), THPC088.

[23] Z. Li *et al.*, Physics design of an accelerator for an accelerator-driven subcritical system, Phys. Rev. ST Accel. Beams **16**, 080101 (2013).

[24] Mengxin Xu, Status and challenges of Nb/Cu SRF cavities for superconducting linac, in *Proceedings of 31st International Linear Accelerator Conference, LINAC2022, Liverpool, UK* (JACoW, Geneva, Switzerland, 2022), TU1AA01.

[25] Weiming Yue, Shengxue Zhang, Chunlong Li *et al.*, Development of a low beta half-wave superconducting cavity and its improvement from mechanical point of view, Nucl. Instrum. Methods Phys. Res., Sect. A **953**, 163259 (2020).

[26] Yu-Lu Huang, Lu-Bei Liu, Tian-Cai Jiang *et al.*, 650 MHz elliptical superconducting RF cavities for CiADS Project, Nucl. Instrum. Methods Phys. Res., Sect. A **988**, 164906 (2021).

[27] F. Grespan, L. Bellan, M. Comunian Lund *et al.*, Experience from the IFMIF RFQ commissioning, in *Proceedings of ESS Testing and Commissioning Workshop, Lund* (2020).

[28] D. Uriot, TraceWin documentation, http://irfu.cea.fr/Sacm/logiciels/index3.php,2011.

[29] Chuan Zhan, Beam dynamics design, simulation and benchmarking for the C-ADS injector-II RFQ, in *Proceedings of the 4th International Particle Accelerator Conference, IPAC-2013, Shanghai* (JACoW, CERN, Geneva, Switzerland, 2013), THPWO022.

[30] C. Biscari, Computer programs and methods for the design of high intensity RFQs, CERN Report No. CERN/PS 85-67, 1985.

[31] K. R. Crandall, T. P. Wangler, L. M. Young *et al.*, RFQ design codes, Los Alamos National Laboratory Report No. LA-UR-96-1836 (revised), 2005.

[32] Dong-o Jeon, Experimental verification of halo formation mechanism of the SNS front end, *APAC 2007, Indore, India*, WEC3 MA01.

[33] R. Miyamoto, Supplemental study of transverse halo for clarifying MEBT Collimator Functionality (2016), https://docdb01.esss.lu.se/DocDB/0003/000382/001.

[34] Huan Jia, Youjin Yuan, Mingtao Song *et al.*, Design of the MEBT1 for C-ADS injector-II, in *Proceedings of HB2012, Beijing, China* (2012), MOP229.

[35] F. Gerigk, Space charge and beam halos in proton linacs, in *Proceedings of 2002 Joint USPAS–CAS–Japan–Russia Accelerator School, Long Beach, CA* (2002), pp. 257–288.

[36] Z. Li J.-Y. Tang, F. Yan, H.-P. Geng, C. Meng, B. Sun, P. Cheng, Z. Guo, and J.-L. Sun, Longitudinal instability caused by long drifts in the C-ADS injector-I, Chin. Phys. C **37**, 037005 (2013).

[37] F. Gerigk and I. Hofmann, Beam dynamics of non-equipartitioned beams in the case of the SPL project at CERN, in *Proceedings of the 19th Particle Accelerator Conference, Chicago, IL, 2001* (IEEE, Piscataway, NJ, 2001).

[38] I. Hofmann and G. Franchetti, Review of beam dynamics and space charge resonances in high intensity linacs, in *Proceedings of the 8th European Particle Accelerator Conference, Paris, 2002* (EPS-IGA and CERN, Geneva, 2002), pp. 74–78.

[39] I. Hofmann, Stability of anisotropic beams with space charge, Phys. Rev. E **57**, 4713 (1998).

[40] I. Hofmann and O. Boine-Frankenheim, Resonant emittance transfer driven by space charge, Phys. Rev. Lett. **87**, 034802 (2001).

[41] P. N. Ostroumov, V. N. Aseev, and B. Mustapha, Beam loss studies in high-intensity heavy-ion linacs, Phys. Rev. ST Accel. Beams **7**, 090101 (2004).

[42] Jean-Luc Biarrotte and Didier Uriot, Dynamic compensation of an rf cavity failure in a superconducting linac, Phys. Rev. ST Accel. Beams **11**, 072803 (2008).

[43] Bruce Yee-Rendon, Yasuhiro Kondo, Jun Tamura, Keita Nakano, Fujio Maekawa, and Shin-ichiro Meigo, Beam dynamics studies for fast beam trip recovery of the Japan Atomic Energy Agency accelerator-driven subcritical system, Phys. Rev. Accel. Beams **25**, 080101 (2022).

[44] J-L.Biarrotte, Beam dynamics studies for the fault tolerance assessment of the PDS-XADS linac design, in *Proceedings of the 9th European Particle Accelerator Conference, Lucerne, 2004* (EPS-AG, Lucerne, 2004), pp. 1282–1284.

[45] J. Galambos *et al.*, Operational experience of a superconducting cavity fault recovery system at the spallation neutron source, in *Proceedings of the Fifth International Workshop on the Utilisation an Reliability of High Power Proton Accelerators, Mol, Belgium* (2007).

[46] Jia Yongzhi, H. E. Yuan, Wang Zhijun *et al.*, Piecewise compensation and redundancy design for superconducting cavity failure of CiADS Linac, Nucl. Phys. Rev. **34**, 62 (2017).